Reservoir permeability mapping using microearthquake data

CrossMark

Yi Fang[a,*], Derek Elsworth[a,b], Trenton T. Cladouhos[c]

[a] Department of Energy and Mineral Engineering, EMS Energy Institute, and G3 Center, The Pennsylvania State University, University Park, PA 16802, United States
[b] Department of Geosciences, EMS Energy Institute, and G3 Center, The Pennsylvania State University, University Park, PA 16802, United States
[c] AltaRock Energy, Inc., Seattle, WA, 98103, United States

ARTICLE INFO

ABSTRACT

Evaluating hydraulic properties of fractured reservoirs both during and after stimulation is vital for the development of Enhanced Geothermal System (EGS). To constrain the evolution of fracture permeability at sufficiently fine resolution to define reservoir response, we propose a model that couples the moment magnitude to fracture aperture and then estimates the reservoir permeability at relatively high resolution. The critical parameters controlling fracture aperture and permeability evolution are stress-drop, the bulk modulus of the fracture embedded matrix, and the dilation angle of fractures. We employ Oda's crack tensor theory and a cubic-law based analog to estimate the permeability of a synthetic fractured reservoir at various scales, demonstrating that the resolution of permeability is largely determined by the cellular grid size. These methods are applied to map the in-situ permeability of the Newberry EGS reservoir using observed microearthquakes (MEQs) induced during two rounds of reservoir stimulations in 2014. The equivalent mean permeability evaluated by each method is consistent and unlimited by representative elementary volume (REV) size. With identical parameters, Oda's crack tensor theory produces a more accurate estimation of permeability than that of the cubic law method, but estimates are within one order of magnitude. The permeability maps show that the most permeable zone is located within the zone of most dense seismicity, providing a reference for the siting of the production well. This model has the potential for mapping permeability evolution from MEQ data in conventional and unconventional resources and at various scales.

1. Introduction

Some unconventional resources, such as geothermal energy, have the potential to enable a transition to a more sustainable energy future. Enhanced Geothermal Systems (EGS) have the potential to tap the Earth's vast thermal resource. Since fractures are the most abundant structural feature in the upper crust (Warren and Root, 1963) and a fracture surface may have much higher permeability than the surrounding rock matrix and therefore operate as a conduit for fluids, a key capability for the successful development of EGS is to generate sufficient permeability in naturally fractured reservoirs via hydroshearing and to optimally accommodate the production well according to the identified locations of clustered fractures (Rinaldi et al., 2015; Cladouhos et al., 2016). Traditionally, information on fracture attributes has come from well data (Barthélémy et al., 2009; Zeeb et al., 2013), but for reservoirs undergoing active stimulation at a greater depth, microseismic monitoring is the most effective and useful method to characterize the spatial distributions of fractures as well as fluid migration in the subsurface (Maxwell and Urbancic, 2001; Maxwell et al., 2010; Downie et al., 2013). This reservoir feedback occurs since the injected fluid reactivates pre-existing fractures and thus triggers microearthquakes (MEQs) (Nicholson and Wesson, 1990; Majer et al., 2007; Suckale, 2009; Ellsworth, 2013; Guglielmi et al., 2015). Hence it is of particular interest to evaluate the properties of fractures and to estimate the evolution of permeability – it has become essential and necessary to establish a model that accurately captures the hydraulic properties using the crucial feedback on stimulation contained within the observed MEQs.

A number of previous studies have provided insight into connections between in-situ MEQ data, inferred subsurface fluid migration and reservoir state. For example, the hydraulic diffusivity may be defined from the analysis of the spatio-temporal growth of the fluid-injection-induced seismic cloud (Shapiro et al., 1997, 2006). If the leading edge of the seismic cloud is presumed coincident with the fluid pressure front, then fluid diffusivity may be evaluated at reservoir scale (Hummel and Shapiro, 2012). However, this method ignores local geomechanical effects and variations in fracture permeability caused by hydroshearing. As a result, it cannot constrain permeability at finer

---

Nomenclature

a^*	Frictional parameter (direct effect)
A	Area of the fracture surface
b	b-value
b^*	Frictional parameter (evolution effect)
b_f	Fracture aperture
b_m	Mechanical aperture at low reference stress
b_n	Normal aperture
b_{nIni}	Normal aperture before fluid injection
b_{nFin}	Normal aperture after fluid injection
b_r	Residual aperture
b_s	Shear aperture
c_n	Contribution coefficient of tensile failure
c_s	Contribution coefficient of shear failure
D_p	Reservoir depth
e	Power-law scaling exponent
E	Young's modulus
F_{ij}	Fabric tensor
G	Average shear modulus of fracture embedded rock mass
k_{ij}	Permeability tensor
k_m	Mean permeability
k_{matrix}	Matrix permeability
k_T	Source-type parameter
k_{tot}	Total mean permeability
k_{aseis}	Mean permeability of aseismic fracture networks
k_{seis}	Mean permeability of seismic fracture networks
K	Bulk modulus
K_{IC}	Stress intensity factor
K_s	Fracture stiffness
l	Fracture trace length
l_h	Fracture radius or half length
L_{rev}	Scan line or imaginary grid size (REV size)
M	Moment tensor
M_0	Seismic moment
M_0^s	Seismic moment for pure shear failure
M_0^n	Seismic moment for pure tensile failure
M_w	Moment magnitude
n	Number of fracture
$\boldsymbol{n}$	Unit vector of the fracture plane
N_{tot}	Total population of fractures
N_{aseis}	Population of aseismic fractures with size less than critical length
N_{seis}	Population of seismic fractures
N_f	Number of activated fractures
N_{uf}	Number of unactivated fractures
P_0	Initial hydrostatic pore pressure
P_f	Total fluid pressure
P_f^{crt}	Critical fluid pressure at which the pre-existing fracture is reactivated
P_w	Wellhead pressure
P_{wf}	Minimum wellhead pressure required to reactivate pre-existing fractures
$\bar{S}$	Average fracture spacing
S_{aseis}	Spacing of aseismic fractures
S_{seis}	Spacing of seismic fractures
S_f	Fracture spacing
S_H	Maximum horizontal stress
S_h	Minimum horizontal stress
S_v	Vertical stress
S_1	Maximum principal stress
S_3	Minimum principal stress
Δu_{max}	Maximum final dislocation for 100% stress drop
Δu_n	Average normal opening
Δu_s	Average shear displacement
V_{rev}	Representative elementary volume
V_0	Reference velocity
V_f	Coseismic velocity
α_f	Pre-factor of aperture-to-length scaling law
α_s	Stiffness parameter
ρ_{frac}	Density of centers of fracture planes
ρ_c	Density constant in fracture length-frequency power law
δ_{ij}	Kronecker delta
η	Fracture geometric factor
θ	Fracture orientation
λ	Nondimensional coefficient
μ_s	Static friction coefficient
$\Delta\mu$	Frictional drop
ν	Poisson's ratio
ξ	Exponent in the fracture length-frequency power law
σ_n	Normal stress
σ_n^{crt}	Critical normal stress at which the pre-existing fracture is reactivated
τ	Shear stress
$\Delta\tau$	Stress drop
$d\Omega$	Solid angle
ψ	Dilation angle

resolution. In addition, a viable approach estimates a linkage between triggering fluid pressures and in-situ MEQ data (Terakawa et al., 2010, 2012). This method integrates focal mechanism tomographic techniques and the Mohr-Coulomb failure criterion to indicate the fluid pressure along the fracture plane at the time of slip. Though this work provides constraint of a 3D distribution of fluid pressures in the stimulated zone of the reservoir, it does not include the contribution of the fracture network to the evolution of hydraulic properties (*i.e.,* permeability heterogeneity) that are of principal interest for long-term EGS production. Meanwhile, Ishibashi et al. (2016) have tried to link the microseismicity to the permeability evolution by considering the topography of fracture/fault surfaces.

In the following, we propose a model to couple in-situ MEQ data and in-situ permeability at various reservoir scales. This model assumes that induced seismicity is controlled by the Mohr-Coulomb failure criterion and applies the moment magnitude of MEQs to recover fracture shear slip (Stein and Wysession, 2009). We explore two alternate approaches – (1) the cubic law based equivalent porous-medium method (EPM) and (2) Oda's crack tensor theory (*i.e.*, discrete fracture network

(DFN)) to approximately define the permeability at a suitable representative elementary volume of the reservoir (REV).

The cubic law may be used to link permeability of the reservoir to the aperture of fractures, as a fundamental parameter that, in turn, may be indexed to seismicity. As fluid is usually channeled in permeable fractures that occupy only a small volume of the rock mass, it is important to characterize such hydraulic properties with consideration of the appropriate length scale. The hydraulic properties of the fracture network are captured as an equivalent permeability (Snow, 1969; Tsang and Witherspoon, 1981) for parallel or ubiquitous joints. An alternate approach is to use a discrete fracture model (Oda, 1982) in the evaluation of permeability. Thus a model-fabric tensor may be used to describe the geometric characteristics of fractured rock and to determine transport characteristics (Oda, 1982, 1984).

In this study, we are primarily interested in the sensitivity of parameters that control stress state and fracture properties, and their significance in influencing the moment magnitude of MEQs and the evolution of permeability before and after seismic slip. We use a synthetic model to explore the features of the two methods and indicate the

most significant factors that dominate the resolution of the evaluated permeability. The significance of this model lies in two aspects: (1) it allows abundant observations of MEQs to constrain the structure and distribution of in-situ permeability evolution of the reservoir; and (2) it reinforces the importance of determining high fidelity in-situ geomechanical parameters (*e.g.*, fracture orientation, fracture stiffness, dilation and friction) and moment tensors, as crucial in successfully constraining permeability evolution.

2. Methods

In the following, we first identify the assumptions and define the key features of the model, and use these to provide the rationale to recover the physical relations that couple both cubic law based equivalent porous medium method and Oda's crack tensor theory to the hydraulic behavior of fractures. The detailed coupling mechanism is introduced in Appendix A.

2.1. Assumptions

Naturally fractured reservoirs are complex and difficult to characterize due to the significant uncertainty in the subsurface. Experimental observations provide some constraints on the fluid-mechanical coupling (Elsworth and Goodman, 1986; Polak et al., 2003) as illustrated in Fig. 1. Key concepts include that: **(1)** the seismicity induced by hydroshearing of fractures is controlled by the Mohr-Coulomb shear failure criterion. **(2)** The frictional coefficient of fractures evolves during seismic slip; in a seismic event, a velocity weakening fracture slips while friction drops from a static to a dynamic value. **(3)** In the reservoir, two types of fractures are considered **(i)** seismic fractures and **(ii)** aseismic fractures – the latter being fractures smaller than a critical

radius such that stick slip cannot be triggered by increased fluid pressure and "failure" proceeds aseismically (Fang et al., 2015). However, aseismic slip may also contribute to the permeability change of fractures (Guglielmi et al., 2015), but its occurrence may not be on the same scale or timeframe of the reservoir stimulation (Peng and Gomberg, 2010). In addition, fractures that slip seismically, but whose signal is below the recording threshold of $M_w < 0.0$ will not be recorded. For the stress drop selected here, these missing fractures have a radius less than ∼10 m **(4)** Neighboring fractures are mechanically isolated and do not interact. The direction and magnitude of the maximum principal stress (total stress) applied to the population of fractures remains unchanged.

2.2. Equivalent porous medium method

Pre-existing natural fractures are the most abundant structures in EGS reservoirs where fractures play a governing role in defining the hydraulic evolution of the reservoir (Murphy et al., 1981; Breede et al., 2013). The reservoir may be represented as an equivalent dual-porous medium with orthogonal fractures as illustrated in Fig. 1**(b)**. The equivalent permeability of a rock mass can be expressed using the cubic law as (Witherspoon et al., 1980):

$$k_m = \frac{b_f^3}{12 S_f} \tag{1}$$

where k_m, b_f, S_f are permeability, fracture aperture, and fracture spacing, respectively. As an important attribute of natural fracture systems, the fracture spacing can be problematic to estimate in the subsurface. Several methods of estimating fracture spacing have been previously introduced (Priest et al., 1976; Priest and Hudson, 1981; Bour and
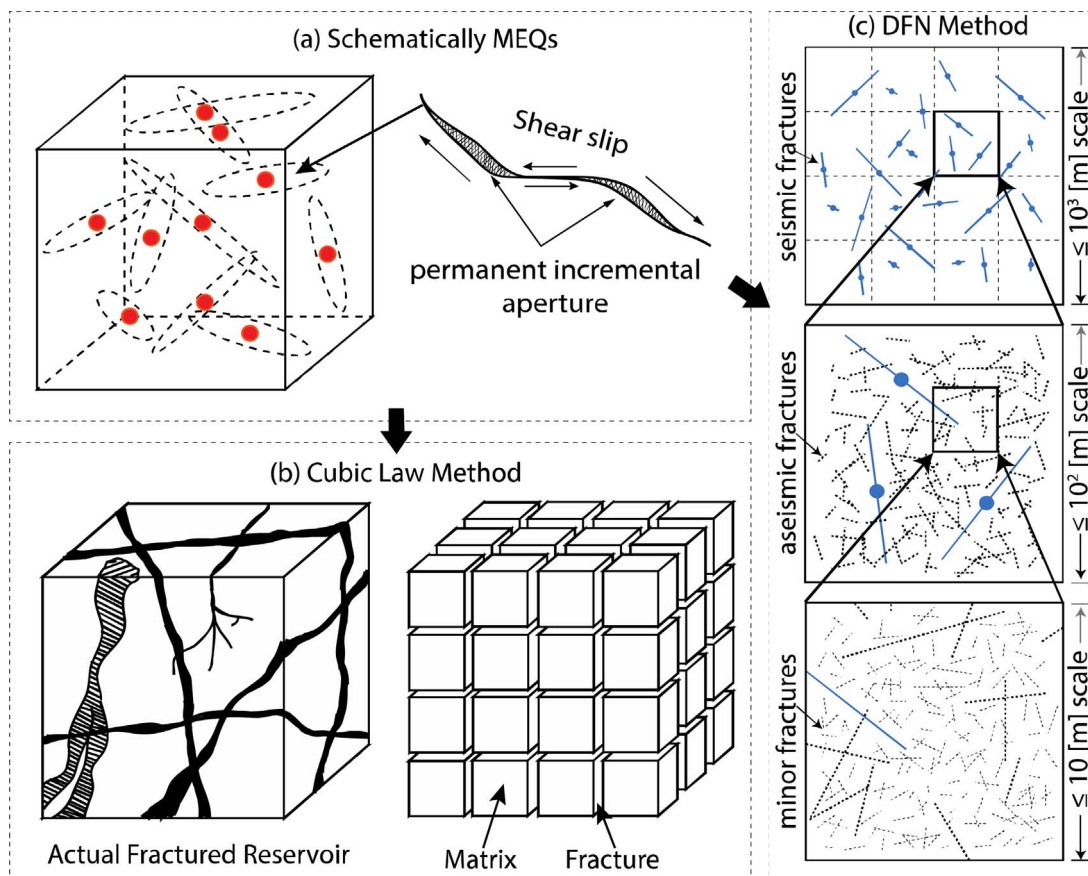

Fig. 1. (a) Schematic representation of observed MEQs and shear slip of fractures. **(b)** Equivalent porous-medium models of a heterogeneous fractured reservoir at a defined scale (modified from Warren and Root (1963)). **(c)** Schematic of distributed seismic fractures and aseismic fractures with scales from 10^1 to 10^3 m.

Davy, 1999; Ortega et al., 2006). As spatial variation in permeability is an important feature in this study, we intentionally use a simple scale-dependent approach to measure the average spacing expressed as:

$$\bar{S} = \frac{1}{n} \sum_{i=1}^{n} S_f^i = \frac{L_s}{n} \tag{2}$$

where $\bar{S}$ is the average fracture spacing and n is the number of fractures along a reference scan line length L_s. Because the fracture size can range from microscopic (*e.g.*, microcracks, veins and joints) to regional scales (large-scale joints, dikes and joint networks), we consider the fractures with size smaller than a critical length as aseismic fractures, and separately estimate the equivalent permeability for seismic fracture sets and aseismic fracture sets. These results are then superposed over a representative reservoir volume. Ignoring low-velocity stable sliding effects on the change in aperture of aseismic fractures, we extend Eq. (1) as follows:

$$k_{tot} = k_{seis} + k_{aseis} + k_{matrix} = \begin{cases} \frac{b_{nIni}^3}{12 S_{seis}} + \frac{b_{nIni}^3}{12 S_{aseis}} + k_{matrix} \text{(Before)} \\ \frac{b_{nFin}^3}{12 S_{seis}} + \frac{b_{nFin}^3}{12 S_{aseis}} + k_{matrix} \text{(After)} \end{cases} \tag{3}$$

Where k_{tot} is the total mean permeability; k_{seis} is the mean permeability of the seismic fracture network with fracture spacing S_{seis}; k_{aseis} is the mean permeability of aseismic fracture networks with fracture spacing S_{aseis}; and k_{matrix} is the mean permeability of matrix rock; b_{nIni} is the initial normal aperture of the fracture and b_{nFin} is the final normal aperture after stimulation. In this scenario, S_{aseis} is a constant value assuming an evenly distributed aseismic fracture network in the reservoir while S_{seis} varies with local seismic fracture network density that is defined by the scan line length L_s (*i.e.*, the imaginary mapping grid size).

2.3. Oda's crack tensor theory

If greater details of reservoir fracture attributes (*e.g.*, the fracture size and orientation illustrated in Fig. 1(c)) are available, then Oda's crack tensor theory can be used as an alternative method to map reservoir permeability. In a representative elementary volume V_{rev}, a fabric tensor considers the position, density, shape, dimension and orientation of fractures and averages these features in each arbitrary direction (Oda, 1982, 1984) as

$$F_{ij} = \rho_{frac} \frac{\pi}{4} \int_0^b \int_0^l \int_\Omega l^3 n_i n_j E(\bar{n}, l, b) d\Omega \cdot dl \cdot db \tag{4}$$

where F_{ij} is the fabric tensor; ρ_{frac} is the density of centers of fracture planes in the control volume; $E(\bar{n}, l, b)$ is a probability density function that describes the number of fractures with size (*i.e.*, trace length) in the range l–$(l + dl)$ and with apertures in the range b–$(b + db)$; n is the unit vector to the fracture plane oriented within a small solid angle $d\Omega$. This concept has been extended (Oda, 1985) to represent a permeability tensor based on the assumption that (i) the rock matrix is impermeable and (ii) the fluid is channeled in parallel fracture planes with volumetric flow rate proportional to b^3. Thus the permeability tensor k_{ij} is represented as,

$$k_{ij} = \lambda (P_{kk} \delta_{ij} - P_{ij}) \tag{5}$$

$$P_{ij} = \rho_{frac} \frac{\pi}{4} \int_0^b \int_0^l \int_\Omega l^2 b^3 n_i n_j E(\bar{n}, l, b) d\Omega \cdot dl \cdot db \tag{6}$$

where $\lambda = \lambda(F_{ij})$ is a dimensionless constant associated with fracture interconnectivity and is restricted between 0 and 1/12; δ_{ij} is the Kronecker delta; i and j represent Cartesian coordinate directions x, y, z. For a 2D problem, i and j are defined within x and y. In this method, the flow properties obtained from the fracture models consider the total sum of the areas of the fractures contained in each representative element volume. As fracture aperture is determined by injection pressure, fracture length, moment magnitude, and fracture orientation, the permeability tensor takes an average of all these attributes. For the purpose of comparing the results with EPM method, the mean permeability is calculated from the trace of the permeability tensor in Oda's method.

3. In-Situ MEQ data analysis

According to the physical relations in Fig. A1 in the appendix, we first explore the roles of essential parameters that control the MEQ-permeability coupling. The results of parametric analysis are reported in Appendix B.1. For demonstration purposes, we then define a synthetic discrete fracture network and perform a model study in Appendix B.2. We apply both EPM and Oda methods to estimate the reservoir permeability. Finally we discuss the limitation of the study on the potential application for in-situ data analysis in Appendix B.3.

Differing from the synthetic fracture networks, natural reservoir fracture networks are notably more complex and difficult to
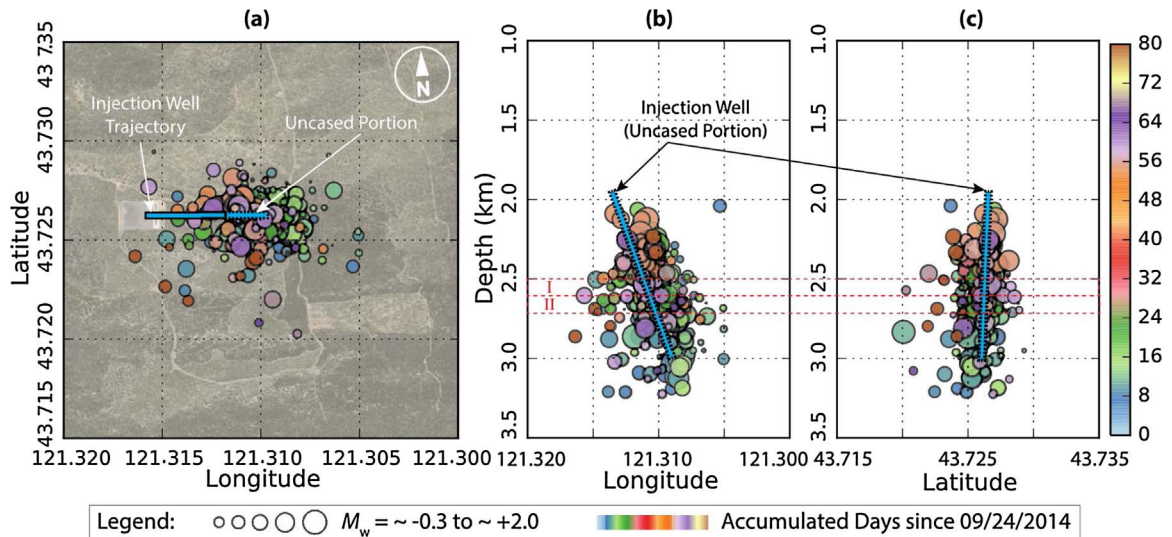

Fig. 2. (a) Map view of the distribution of seismic events in Newberry EGS stimulation (MEQ catalog from LBNL relocations). **(b)** Vertical view of MEQ distribution with Longitude. **(c)** Vertical view of MEQ distribution with Latitude. Circle size shows the magnitudes of MEQ from $M_w = \sim -0.3$ to ~ 2.0 and the color bar highlights the accumulated time since the beginning of the first round stimulation in 2014.

characterize due to the uncertainties of in-situ stress and geologic discontinuities. For in-situ characterization, statistical field measurement of surface outcrops and fracture statistics from borehole imaging are essential and useful methods to reveal correlated fracture structure in near-surface formations. However, microseismic monitoring is the best way to characterize stimulated fracture networks at depth. In this section, we apply the methods introduced in Section 2 and Appendix A to analyze MEQ data from the first two rounds of the 2014 Newberry EGS stimulation (first round from Sept 24th to Oct 15th and second round from Nov 11th to Nov 20th) that followed an earlier 2012 stimulation (Cladouhos et al., 2016; Fang et al., 2015).

3.1. MEQ observations and assumptions

During the 2014 stimulation, about 350 MEQs were located by a fifteen-station microseismic array (Fig. 2) [http://fracture.lbl.gov/Newberry/Location.txt] and the moment tensors analyzed (Julian et al., 1998; Miller et al., 1998). Fig. 3(a) indicates that all of these MEQs were located within a depth range from ~2000 m to ~3300 m while more than 75% of these seismic events occurred within the range ~2500 m to ~3300 m. Among all the MEQs, moment tensors (MT) are available for the 99 events with the best quality and identify the strikes and dip angles of corresponding fault planes. The possibility that these MEQs may be triggered by dynamic stresses associated with distant earthquakes is ruled out (van der Elst and Brodsky, 2010; van der Elst et al., 2013), thus all the MEQs are considered to be the results of the stimulations.

The stress regime is a determining factor that defines the shear failure behavior of the fractures. For the Newberry EGS reservoir we use the normal faulting regime with E-W extension (minimum principal stress) according to World Stress Map. However, the observed focal mechanism solutions show combined double-couple (DC) and non-double-couple (non-DC) results, suggesting a possible strike-slip regime. Due to insufficient evidence to resolve this ambiguity, we use the stress regime aligned with the previous in-situ investigation and related THM simulations (Cladouhos et al., 2011; Davatzes and Hickman, 2011; Fang et al., 2015; Rinaldi et al., 2015). We constrain the vertical σ_v,

maximum horizontal σ_H, and minimum horizontal σ_h, stresses to be zero at the surface and use gradients of 24.1, 23.5 (N-S) and 14.9 (E-W) MPa/km.

To analyze all seismic events, we use these 99 focal mechanism solutions as a statistical reference and randomly assign the strike and dip angle values to non-MT seismic fractures based on a normal distribution. Apparent from Fig. 3(b) and (c), strike orientations of the fractures from the John Day formation share similar ranges with those from the Intruded John Day formation. The dip angles of fractures in the "intruded" John Day formation, in comparison to those in the John Day formation, are more widely distributed.

The observed moment magnitudes of the MEQs are constrained between −0.28 and 2.0 with a *b*-value close to unity. This suggests that the sizes of the seismic fractures in the Newberry EGS reservoir are between meters and one-hundred meters and cannot exceed a thousand meters. Because these observed MEQs do not overprint each other spatially, this implies that each fracture is reactivated once. Thus each distinct seismic event is assumed to represent a pre-existing fracture in the reservoir. The source type, derived from the moment tensors of the observed seismic events in each geologic formation, is displayed on a two dimensional diagram in Fig. 4. The statistical analysis of the source type indicates a negative averaged k_T value (mean = −0.055, standard deviation = 0.18) and suggests a slight volumetric compaction (*i.e.,* fracture closing) of fractures, which seems to contradict the expected dilatational behavior of fracture shearing and volume increase caused by injecting ~ 25000 m^3 of water. We resolve this contradiction by considering the combined effects of perturbation of thermal contraction of the reservoir matrix and the sequential shear compaction and dilation behaviors of fractures. Based on this assumption, we assign a statistically calculated k_T value to the non-moment tensor derived seismic events. Hence we are able to estimate the size of each fracture using Eqs. (A3) to (A10) and Eqs. (A14)–(A21) with the parameters in Table 1. The calculated radii of seismic fractures range from ~ 10 *m* to ~ 150 *m* and are illustrated in Fig. 5(a), agreeing with the widely observed power-law distribution of fracture sizes in natural reservoirs (Bonnet et al., 2001).

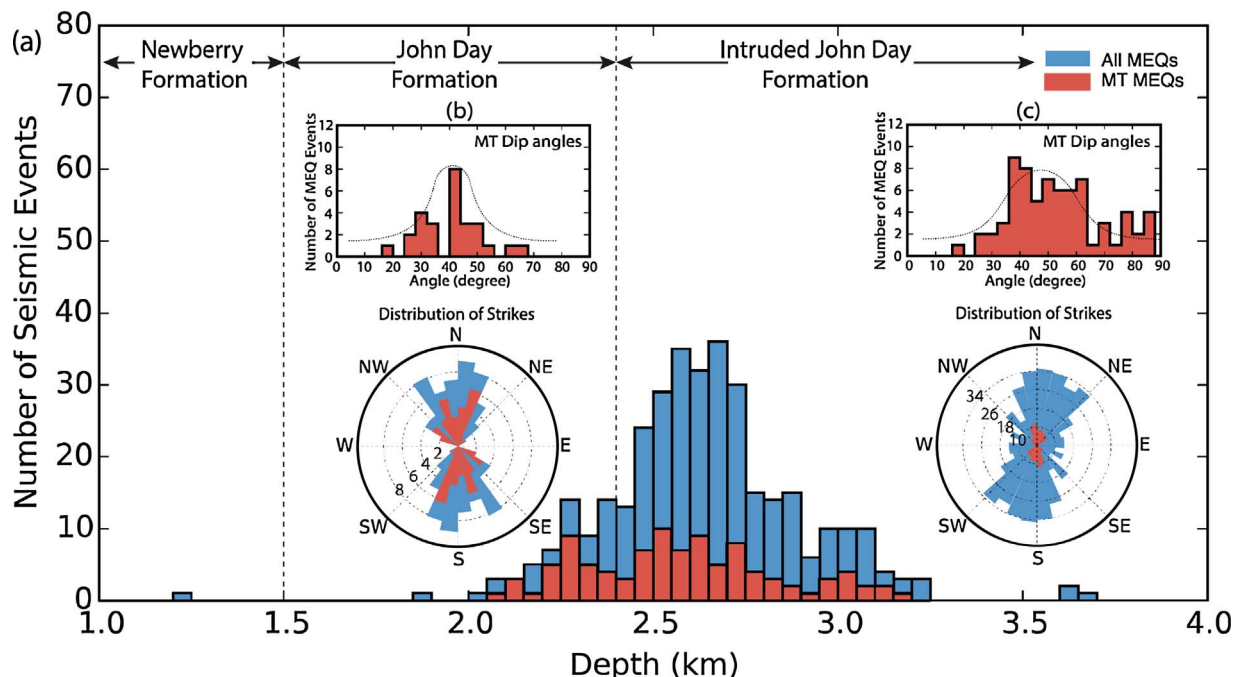We assume that the fluid flow is essentially horizontal and in order

Fig. 3. (a) Histogram of MEQ frequency with depth. Red bars represent the events for which moment tensors are derived. **(b)** Dip angle and strike distribution of fractures in the John Day formation. **(c)** Dip angle and strike distribution of fractures in the "intruded" John Day formation. (For interpretation of the references to colour in this figure legend, the reader is referred to the web version of this article.)
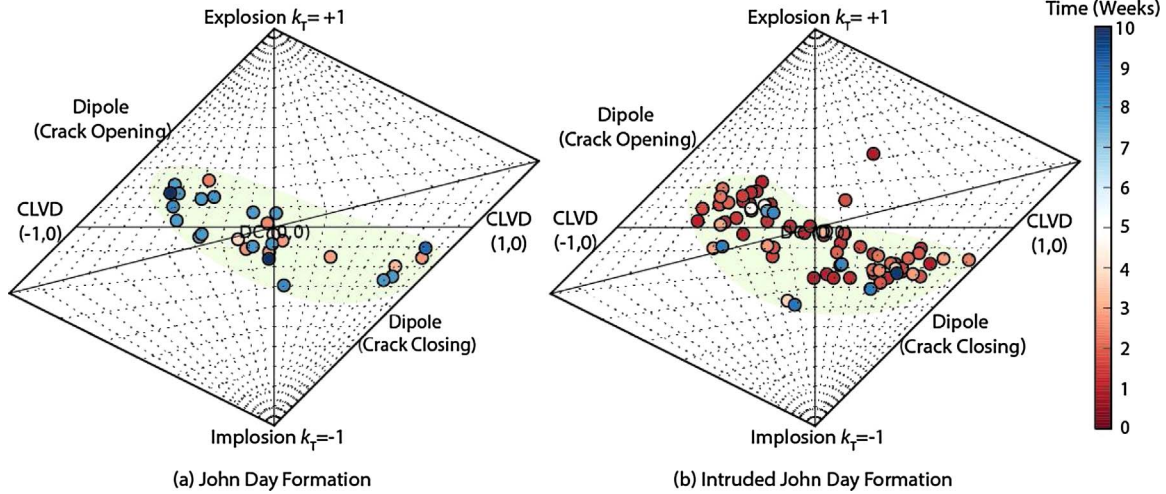
Fig. 4. (a) Source type (k_T value) plot of seismic events in the John Day formation **(b)** Source type plot of seismic events in the "intruded" John Day formation.

Table 1
Parameters used in the in-situ MEQ data.

Parameters	Symbol	Value	Units
Frictional Parameter	$(a^* - b^*)$	0.0005	–
Reference velocity	V_0	1 ~ 2	mm/yr
Coseismic velocity	V_f	1	m/s
Vertical stress gradient	S_v/D_p	24.1	MPa/km
Max-horizontal stress gradient	S_H/D_p	23.5	MPa/km
Min-horizontal stress gradient	S_h/D_p	15.0	MPa/km
Pore-pressure gradient	P_0/D_p	8.8	MPa/km
Residual aperture	b_r	5.0e-5	m
Dilation angle	ψ	5.0	°
Bulk modulus	K	17.0	GPa
Poisson ratio	ν	0.27	–
Non-linear fracture stiffness	α_s	0.218	1/MPa
Power law scaling exponent	e	0.5	m$^{1/2}$
Constant stress intensity factor	K_{IC}	8.0	MPa m$^{1/2}$
REV size	L_{rev}	30	m
Matrix Permeability	k_{matrix}	1.0e-18	m^2
Minor Frac Perm (2500–2600 m)	k_{aseis}	2.6e-16	m^2
Minor Frac Perm (2600–2700 m)	k_{aseis}	2.1e-16	m^2

to analyze spatial variations of permeability in the reservoir, we select two horizontal zones with the highest concentration of seismic events as an example where fracture traces are projected to a plane of zero-thickness (Bundschuh and Arriaga, 2010). The selected zones are constrained to between the depths of 2500 m–2600 m and 2600 m–2700 m respectively, and are bounded by latitude 43.715° to 43.735° and longitude −121.32° to −121.30° as indicated in Fig. 2**(b)** and **(c)**. Compared to the reservoir scale ($\sim 10^3 m$), the lengths of fracture traces

(10^1 m to 10^2 m) are approximately one to two orders of magnitude smaller, suggesting a poor interconnection of these seismic fractures. Due to the low permeability of the rock matrix, there must be abundant pre-existing fractures within the reservoir as fluid conduits and connecting each observed seismic fracture (Fig. 1). These particular small "infill" fractures remain aseismic due to their small size (Scholz, 1998). In this study, the calculated critical fracture radius is ~10 m. Though the accuracy is limited by the seismic sensitivity, the size still appropriately agrees with previous frictional experimental results showing the smallest possible seismic fracture radius to be ~7 m (Fang et al., 2015). Given the total number of seismic fractures N_{seis}, which denotes the number of MEQs in the interval represented by l and $l + dl$, the total number of aseismic fractures is estimated using the power law frequency-length of the fractures as described by Eq. (B1) in the Appendix. Thus the total number of fractures N_{tot} is expressed as follows:

$$N_{tot} = N_{aseis} + N_{seis} = N_{aseis} + N_f + N_{uf} \qquad (7)$$

where N_{aseis} is the population of aseismic fractures with fracture size less than critical length; N_{seis} is the number of seismic fractures including the population (N_f) of activated fractures with favorably oriented fractures and the population (N_{uf}) of unactivated fractures with relatively unfavorably oriented fractures. In this relation, it is noted that when wellhead pressure increases sufficiently, the non-activated fractures convert to "activated" fractures. In Fig. 5**(b)**, the number of non-activated fractures decreases with elevated wellhead pressures and declines to zero at $P_w = \sim 20$ MPa (relaxed with ~5 MPa thermal stress) that is close to the maximum operating wellhead pressure in the field. Over the period of the two rounds of the stimulation, we assume that N_f within the stimulated area has reached a maximum while N_{uf}
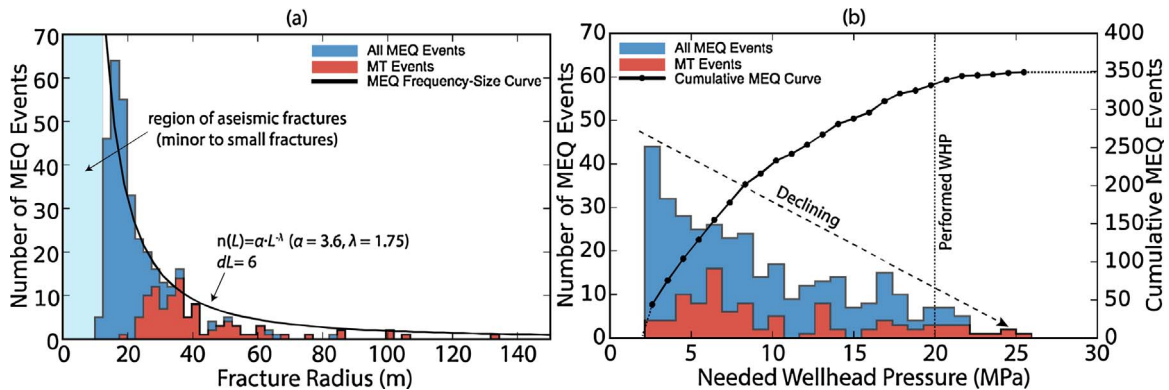

Fig. 5. (a) Size distribution of in-situ fractures calculated from MEQ data. **(b)** Fracture frequency with corresponding required reactivating wellhead pressures (extra fluid pressure).

approaches zero. Thus we set the known number of N_f to be the same as the number of observed MEQs and use the identified power-law distribution to invert for the approximate number of small fractures (aseismic fractures with size smaller than the minimum size limit for unstable slip) within the reservoir. However, the orientation and locations of the sub-seismic fractures are poorly characterized in the Newberry EGS reservoir. As a result, we use a homogeneous Poisson process to define the coordinates of the fracture centers that are uniformly but randomly distributed within the domain as illustrated in Fig. 6(a)–(d). Thus the total reservoir permeability can be regarded as a superposition of seismic fracture permeability, aseismic fracture permeability and matrix permeability using Eq. (3). The presumed matrix permeability

and calculated aseismic/minor fracture permeability of each selected seismic zone are listed in Table 1.

3.2. Results and interpretation

The relation between slip distances of seismic fractures and fracture size is presented in Fig. 6 **(e)**, showing that slip increases linearly (from ~0.1 mm to ~2.1 mm) with growing fracture trace length. Fig. 7 presents the stimulated permeability map of the resulting discrete fractures in Fig. 6, illustrating that the most permeable zone is created adjacent to the injection well in the first round stimulation (northwestern quadrant). After the second stimulation, the permeability is
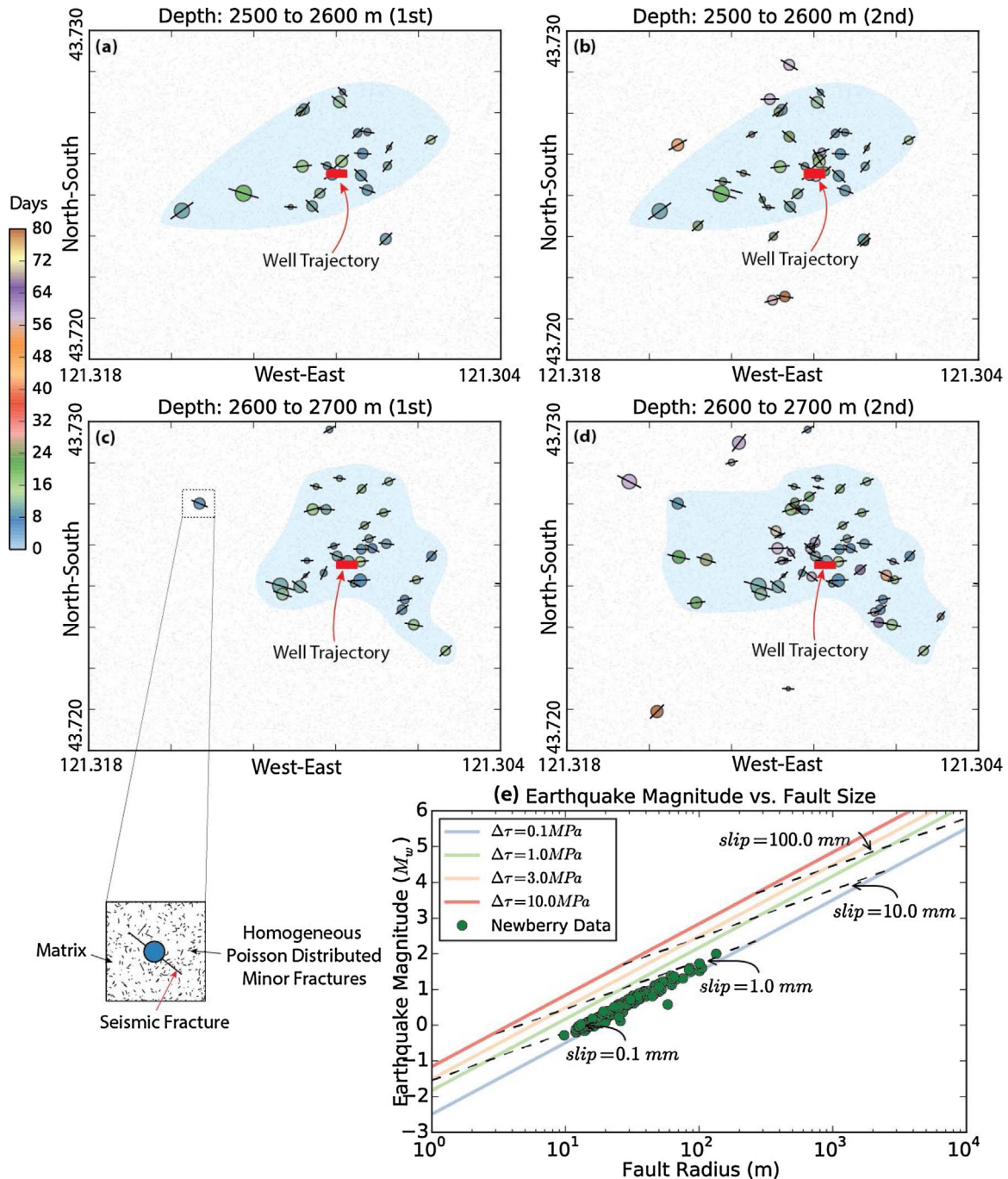

Fig. 6. **(a)** and **(b)** Map view of fracture distributions derived from microseismic events (both 1st and 2nd round stimulation) at a depth of 2500 m to 2600 m. **(c)** and **(d)** Map view of fracture distributions derived from microseismic events (both 1st and 2nd round stimulation) at a depth of 2600 *m* to 2700 *m*. **(e)** Relationship of fracture size and moment magnitude and the corresponding slip distances. Slip distances of fractures in Newberry EGS reservoir labeled as greed dots (Modified from Zoback and Gorelick, 2012 with parameters in Table 1).
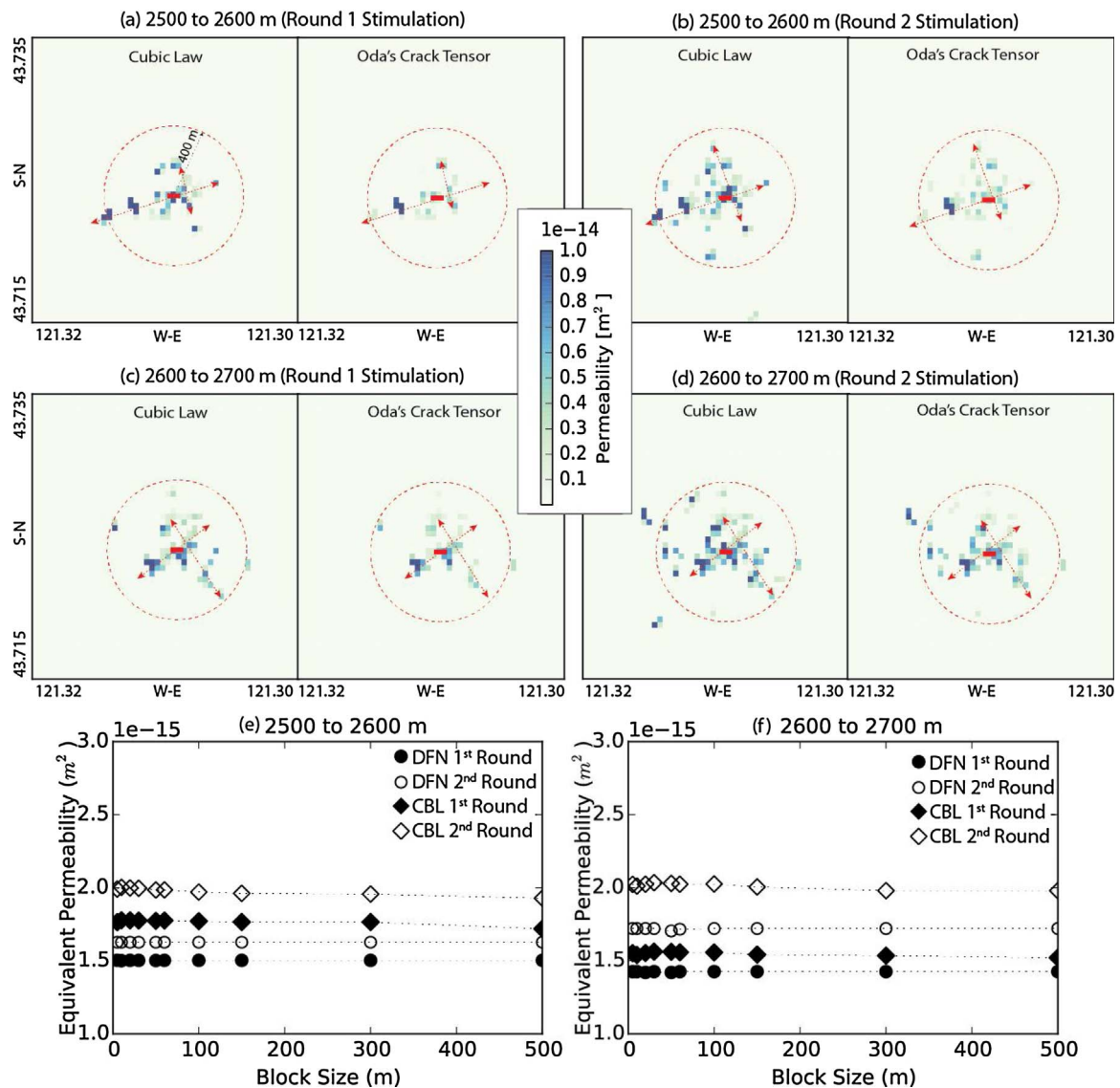
Fig. 7. **(a)–(d)** Celluar grid of stimulated permeability created using both cubic law and Oda's crack tensor methods for both 1st and 2nd round stimulation at a depth of 2500 m to 2600 m and 2600 m to 2700 m respectively. The grid size is 30 m. The effective diffusion length from the injection well is labeled as red circle with a radius of 400 m. **(e)** and **(f)** Comparison of effects of the grid size on the evaluated permeability using both cubic law and Oda's crack tensor methods. (For interpretation of the references to colour in this figure legend, the reader is referred to the web version of this article.)

enhanced around the injection well. In the depth range 2500 m to 2600 m, enhanced permeability develops preferentially towards the southwest while in the depth range 2600 m to 2700 m the trend changes to the southeast. Comparing the mapped cellular permeability recovered by both the cubic law method and by Oda's crack tensor theory, it is expected that the cellular permeability evaluated by the cubic law is slightly higher than that by Oda's crack tensor theory – which is similar to observations within the synthetic reservoir. Thus it is more appropriate to adopt the equivalent mean permeability values estimated by Oda's crack tensor theory. The corresponding estimated equivalent mean permeability of each selected zone at both local reservoir scale (400 m × 400 m) and global reservoir scale (1500 m × 1500 m) are listed in Table 2 and labeled in Fig. 8. Confirmatory and independent estimates of the equivalent mean permeability may be recovered at reservoir scale using pore-pressure diffusion lengths (Shapiro et al., 1997) and the 99 MT events. The diffusion-length versus time curves are shown in Fig. 8, suggesting that the

Table 2
Parameters calculated from the model.

Parameters	Symbol	Value	Units
Frictional drop	$\Delta\mu$	0.012	–
Fracture radius (half length)	l_h	9.79 to 134.25	m
Slide distance	Δu_s	0.1 ~ 2.1	mm
Local Equiv Perm (Zone I, 1st)	k_{local_z1r1}	1.50e-15	m^2
Local Equiv Perm (Zone I, 2nd)	k_{local_z1r2}	1.63e-15	m^2
Local Equiv Perm (Zone II, 1st)	k_{local_z2r1}	1.43e-15	m^2
Local Equiv Perm (Zone II, 2nd)	k_{local_z2r2}	1.72e-15	m^2
Global Equiv Perm (Zone I, 1st)	k_{global_z1r1}	0.34e-15	m^2
Global Equiv Perm (Zone I, 2nd)	k_{global_z1r2}	0.36e-15	m^2
Global Equiv Perm (Zone II, 1st)	k_{global_z2r1}	0.32e-15	m^2
Global Equiv Perm (Zone II, 2nd)	k_{global_z2r2}	0.38e-15	m^2

Note: The local equivalent permeability refers to the permeability averaged over the area of the red dashed circle in Fig. 8 and the global equivalent permeability refers to the permeability averaged over the rectangular area in Fig. 8.
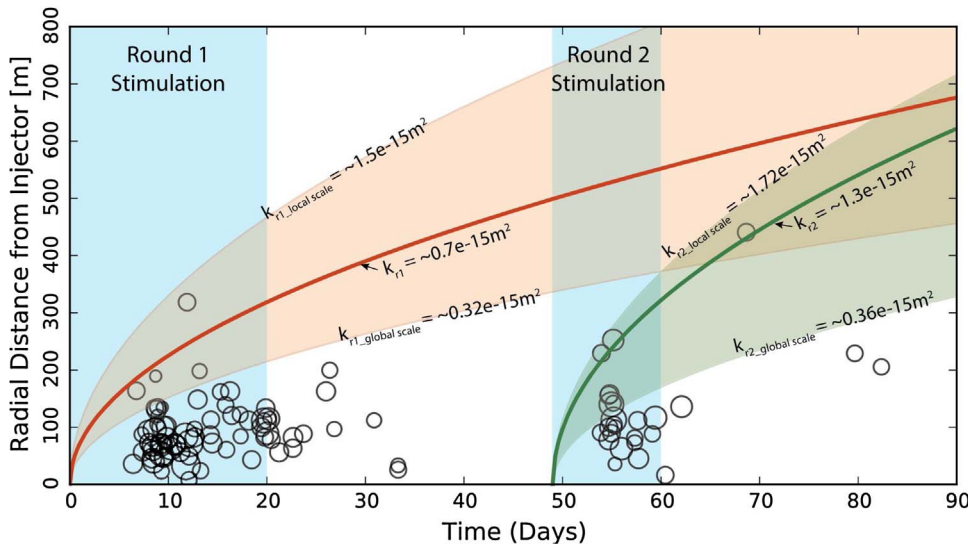
Fig. 8. Spatio-temporal distribution of induced MEQ during the 2014 Newberry EGS stimulation. Diffusion-length versus time curves constrain the equivalent permeabilities at both local and global reservoir scale.

reservoir permeability evolved from $\sim 0.7 \times 10^{-15}\,\text{m}^2$ to $\sim 1.3 \times 10^{-15}\,\text{m}^2$ which are bounded by the estimated permeability values.

4. Conclusion

In this work we present a model that links observed MEQs to the permeability of the fractured reservoir. The model links the established physical coupling between hydraulic and mechanical properties of fractures, hydroshearing-induced seismicity, and fracture permeability. We first investigate all the controlling parameters in the governing equations and define the most significant geophysical properties that determine the aperture of the fracture, for example, frictional evolution, fracture dilation angle, moment magnitude and the distribution of spatial seismicity (*i.e.* fracture populations, locations, spacing) and apply both the cubic law and Oda's crack tensor theory to a synthetic reservoir model as a demonstration. We then evaluate the permeability distribution and its evolution using MEQ data from the stimulation of the Newberry EGS reservoir. Comparison of predicted permeabilities derived from each method identifies that **(1)** the resolution of permeability is largely determined by the cellular grid size and the fracture size for both Oda's crack tensor theory and cubic law methods while the

evaluated equivalent permeability is independent of the limitation of the REV size. **(2)** With identical parameters, although Oda's crack tensor theory produces a more accurate estimation of permeability than that of the cubic law, the difference between the two estimates is less than one order magnitude. **(3)** In the reservoir, the most permeable zone is located within the densest zone of MEQs. This model has potential application for mapping permeability evolution using in-situ monitored MEQ data in both conventional and unconventional reservoirs at various scales. The study also suggests that higher reliability of the results can be achieved through improving the accuracy of the parameters that are used in the model. Particularly in practical operations, the quality of the observed moment tensors recovered through microseismic monitoring is key in determining the accuracy of the properties of the in-situ fractures and the recovered permeability of the EGS reservoir.

Appendix A. Mechanism of MEQ-permeability coupling

In Eqs. (3) and (6), the fracture aperture is an essential parameter in both the EPM and DFN (Oda) methods for estimating the permeability. Thus the central requirement for MEQ-permeability coupling is to correlate the fracture aperture to the moment magnitude. When pre-existing fractures are reactivated, the aperture changes due to the combined effects of normal opening, shear dilation and thermal expansion/contraction. It may be expressed as an integration of nonlinear normal stress-dependent aperture b_n and shear stress-dependent aperture b_s (Rutqvist and Tsang, 2003; Rutqvist et al., 2004) as,

$$b = b_n + b_s \tag{A1}$$

$$b_n = b_r + (b_m - b_r)\cdot \exp[-\alpha_s\cdot(\sigma_n - P_f)] \tag{A2}$$

where b_r is the irreducible or residual aperture at maximum mechanical loading; b_m is the mechanical aperture under a small reference stress or zero stress; the difference of b_r and b_m is the maximum opening b_{max}; α_s [1/MPa] is the stiffness parameter determined from experiments; σ_n is the remote normal stress perpendicular to the fracture surface; and P_f is the internal fluid pressure in the fracture.

In this work, the local normal stress σ_n on the fracture plane can be determined via principal stresses at depth as,

$$S = diag[S_1, S_2, S_3] \tag{A3}$$

with stresses in a local coordinate system obtained by tensor transformation as,

$$S_G = R_G^T\cdot S\cdot R_G \tag{A4}$$

where R_G is the rotation matrix. Hence, the normal stress on a fault plane coordinate system can be calculated as,The shear stresses τ_d and τ_s are defined in terms of both dip and strike directions as,where $\hat{n}$, $\hat{n}_d$, $\hat{n}_s$ are vectors defined by the strike and dip angle of fracture planes.

According to the Mohr-Coulomb failure criterion, we assume that shear failure of a pre-existing fracture occurs at the critical normal stress σ_n^{crt} and critical fluid pressure $P_f = P_f^{crt}$, expressed as,

$$P_f^{crt} = \sigma_n - \tau/\mu_s \tag{A8}$$

$$\sigma_n^{crt} = \sigma_n - P_f \tag{A9}$$

$$P_{wf} = P_f^{crt} - P_0 \tag{A10}$$

where τ is the magnitude of total shear stress acting on the fracture plane; μ_s is the static frictional coefficient of the fracture; P_{wf} is the minimum wellhead pressure required to reactivate pre-existing fractures and P_0 is the hydrostatic pore pressure of the reservoir before the injection of fluids. When the increased fluid pressure triggers fracture reactivation, the shear aperture b_s will increase and its magnitude is controlled by the slip distance Δu_s and fracture dilation angle ψ, as,

$$b_s = \Delta u_s \cdot \tan\psi \tag{A11}$$

The maximum aperture opening is predicted using a sublinear aperture-to-length scaling law, postulating that fractures of different lengths preserved in a homogenous body of rock are all in the same condition (i.e., constant stress intensity K_{IC}) (Olson, 2003). The law is expressed as:

$$b_m = \alpha_f \cdot l_h^e \tag{A12}$$

$$\alpha_f = \frac{K_{IC} \cdot (1 - \nu^2)}{E \cdot \sqrt{\pi/8}} \tag{A13}$$

where α_f is the pre-factor defined by the constant stress intensity factor K_{IC} with units of m^{1-e}, Young's modulus E, and Poisson's ratio υ; l_h refers to fracture radius or half length; and e is the power-law scaling exponent. However, the shear aperture component b_s is only applicable when shear failure occurs during a seismic event. If fluid pressure is insufficient to induce shear failure on fractures, the permeability evolution is dominated by the effective normal stress. When shear failure occurs, seismic energy M_0^s (seismic moment) is released during shear slip. The seismic moment is determined from the moment tensor M of individual seismic events and can be further correlated to the moment magnitude as,

$$M_0 = M_0^s = G \cdot A \cdot \Delta u_s \tag{A14}$$

$$M_w = \frac{2}{3}(\log M_0 - 16.1) \tag{A15}$$

where G is the average shear modulus of the fracture embedded within the rock mass, A is the area of the fracture surface, and Δu_s is the average displacement over the entire fracture surface quantified as (Brune, 1970),

$$\Delta u_s = \frac{2}{3}\Delta u_{\max} = \frac{2}{3} \cdot \frac{\Delta\tau}{K_s} \tag{A16}$$

$$\Delta\tau = \Delta\mu \cdot \sigma_n^{crt} \tag{A17}$$

$$K_s = \frac{G \cdot \eta}{l_h} \tag{A18}$$

where $\Delta u_{\max}$ is the maximum final dislocation for 100% stress drop $\Delta\tau$; K_s is the fracture stiffness; l_h is the fracture radius; assuming that fractures in the reservoir are penny-shaped, thus the geometric factor η has the value of $7\pi/24$ (Dieterich, 1986, 1992); $\Delta\mu$ is the frictional change in shear slip and can be further extended as,

$$\Delta\mu = |a^* - b^*| \cdot \ln\left(\frac{V_f}{V_0}\right) \tag{A19}$$

where $(a^* - b^*)$ is the frictional parameter (i.e., $(a^* - b^*) < 0$ for velocity weakening and $(a^* - b^*) > 0$ for velocity strengthening), V_f is the coseismic shear velocity ($\sim 10^0$ m/s to 10^2 m/s) of fractures, and V_0 is the reference velocity or background velocity (~ 1 to 2 mm/yr) of fractures.

In reality, the moment tensor of observed MEQs in EGS reservoirs may indicate mixed failure modes (Julian et al., 1998; Miller et al., 1998). The focal mechanism solutions of these events show combined double-couple (DC) and non-double-couple (non-DC) components, suggesting both fracture shearing and opening/closing and making the estimation of fracture size more difficult. To simplify the complexity, we define two end-member MEQ scenarios: (i) pure double-couple MEQs as a result of pure shear failure, in which the seismic moment can be expressed by Eq. (A14) and (ii) pure non-double-couple MEQs due to pure tensile failure where the seismic moment is defined as follows (Foulger and Long, 1984),

$$M_0 = M_0^n = 2G \cdot A \cdot \Delta u_n \tag{A20}$$

where Δu_n refers to the normal displacement of crack opening or closing. Most fracture deformations occur between these two end-members. To quantify the deformational contribution from each end-member, Hudson et al. (1989) defines the source-type parameter k_T as the measure of the relative size of the dilatational component of the moment tensor. Assuming a linear decomposition from the seismic moment, the quantitative relation of the two end-member MEQ scenarios can be defined as,

$$M_0 = M_0^s + M_0^n = c_s \cdot M_0 + c_n \cdot M_0 = G \cdot A \cdot (c_s \cdot \Delta u_s + 2c_n \cdot \Delta u_n) \tag{A21}$$

$$c_s = 1 - |k_T| \tag{A22}$$

$$c_n = |k_T| \tag{A23}$$

where parameters c_s and c_n denote the contributions from each end-member MEQ mode and parameter k_T ranges between -1 to 1. In this case, the fracture is assumed to be in opening when k_T is greater than 0 and in closing when k_T is smaller than 0 (Hudson et al., 1989).

These prior physical relations (*i.e.*, Eqs. (A1)–(A21)) are schematically illustrated in Fig. A1. The spatial distribution of MEQs can imply local stress magnitudes on fractures if reservoir stress gradients are well constrained. The reservoir stress state and reservoir material properties, which control the fracture properties, can be quantitatively correlated to MEQ magnitudes by fracture size. As a result, the permeability enhancement resulting from shear slip or crack opening during EGS stimulation can be estimated.
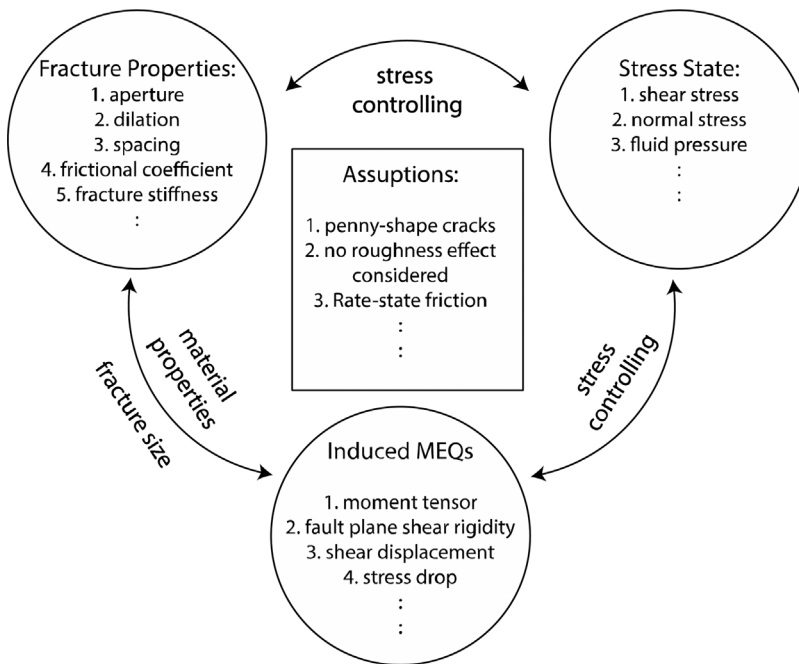
Fig. A1. Schematic of relations among physical properties and variables that controlling MEQ-permeability coupling.

Appendix B. Model study

B.1 Parametric analysis

The physical relations described in Appendix A involve parameters that may influence the variations of the hydraulic properties of fractures. These geomechanical controls can be attributed to both normal and shear stress effects on the fracture aperture and permeability. To understand how sensitive the permeability evolution of fractures is to these parameters, and the potential effects of these sensitivities on the interpretation of the *in-situ* MEQ data, we perform a parametric study on permeability evolution of fractures with radius from 1 *m* to 1000 *m* at a depth of 3 *km*. The values of parameters are listed in Table B1. The fractures are assumed to fail in shear.

First, a log-linear relationship between seismic moment magnitude (M_w) and the fracture size is indicated in Fig. B1. For a fracture with a fixed orientation (defined by θ), a larger frictional drop results a larger moment magnitude. If the frictional drop is fixed, shear slip of a fracture with a favorable orientation induces a slightly larger moment magnitude than that of unfavorably oriented fractures. Since friction is a function of the minerals comprising the fractures (Ikari et al., 2011; Fang et al., 2015) and the fracture orientation (*i.e.*, strike and dip) can be partially reflected through the moment tensor, it can be speculated that, for a precisely calculated seismic moment magnitude and a well-determined fracture orientation, an accurately measured frictional change can reduce the error in calculating the fracture size.

Table B1
Ranges of Values Used in *Parametric* Study.

| Parameters	Symbol	Value	Units
Fracture radius	l_h	1–1000	m
Frictional drop	$\Delta\mu$	0.05, 0.10, 0.15	–
Maximum Principal Stress	S_1	72.0	MPa
Minimum Principal Stress	S_3	45.0	MPa
Pore-pressure	P_0	30.0	MPa
Residual aperture	b_r	5.0e-5, 1.0e-4, 1.5e-4	m
Dilation angle	ψ	1, 5, 10	°
Bulk modulus	K	15, 20, 25	GPa
Poisson ratio	ν	0.25	–
Non-linear fracture stiffness	α_s	0.3	1/MPa
Power law scaling exponent	e	0.5	m$^{1/2}$
Constant stress intensity factor	K_{IC}	5, 10, 15	MPa m$^{1/2}$
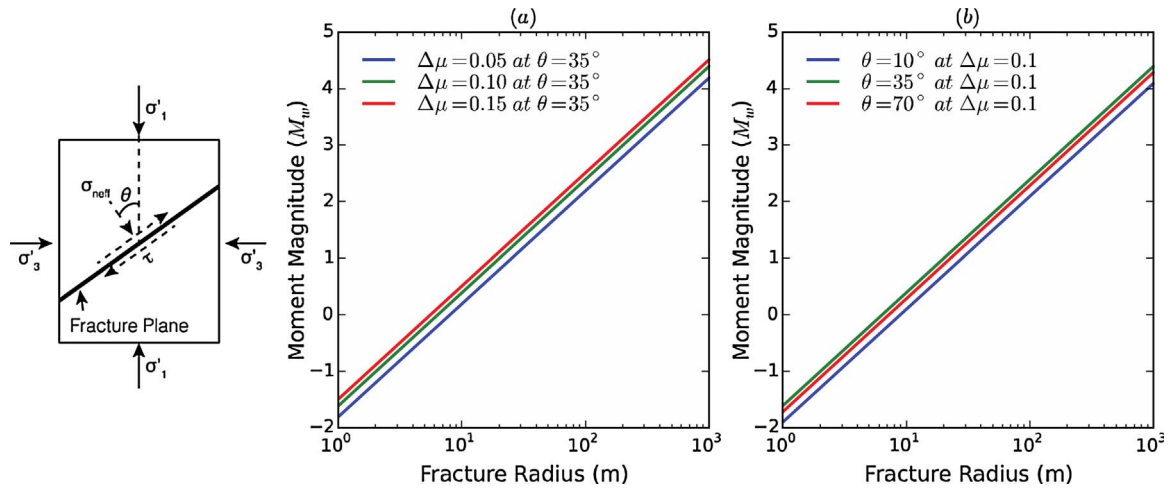
Fig. B1. Log-linear relationship between seismic moment magnitude (M_w) and the fracture size for a single fracture: **(a)** Effect of frictional difference $\Delta\mu$ on moment magnitude M_w; **(b)** Effect of localized orientation of fracture (defined as the angle between fracture plane normal and direction of maximum principal stress) on moment magnitude M_w. The stresses are listed in Table B1.

The variation of fracture aperture with respect to fracture radius may be defined. The initial aperture and evolving aperture of fractures without shear failure, termed b_{ini} and b_n respectively, are controlled by the fluid pressure that acts on the fracture walls and enlarges the normal aperture of fractures. When the fluid pressure reaches the critical magnitude P_f^{crt} and the shear stress acting on the fracture exceeds its strength, shear slip occurs, resulting in an enhancement of aperture, b_s. Therefore, the fluid pressure plays a role as a trigger for seismic slip. According to Eqs. (A9), (A16) and (A17), the magnitude of the shear aperture b_s is constant when the fluid pressure reaches and exceeds a critical value. Changes in normal aperture and to permeability are largely reversible in the elastic loading and unloading cycle. When fluid pressure is dissipated, the reduced changes in normal aperture are negligible compared to those changes in the aperture that are permanently enhanced by shear slip. Hence, the fluid pressure is an important factor in triggering failure but exerts less significant control in the evolution of permanent aperture. In addition to fluid pressure, the following parameters may affect the evolution of aperture in normal, b_n and in shear, b_s modes as separated into three categories: (1) reservoir deformability characteristics, for example, the bulk modulus K of the reservoir; (2) fracture deformability characteristics, such as residual aperture b_r and dilation angle ψ; and (3) fracture material properties, such as fracture toughness K_{IC} and frictional drop $\Delta\mu$. As presented in Fig. B2**(a)** and **(b)**, both the bulk modulus K and the fracture toughness K_{IC} have little effect on the normal aperture b_n, particularly for fracture radii less than $\sim 10\ m$. The effect of residual aperture b_r on normal aperture is apparent in comparing results for both K and K_{IC} (Fig. B2**(c)**). From Fig. B2**(d)–(f)**, the change in aperture due to shear slip of fractures larger than $\sim 10^2\ m$ is mainly controlled by the bulk modulus K, the shear dilation angle ψ and the frictional drop $\Delta\mu$. In summary, the physical linkage between the moment magnitude of seismic events and the fracture aperture is most strongly influenced by the controlling factors of frictional drop, fracture dilation angle, and fracture embedded bulk modulus that define the magnitudes of stress drop, shear deformation and the resistance to shear deformation respectively. However, these parameters have only a limited effects on small fractures ($< 10\ m$) where the corresponding moment magnitude is less than ~ 0 to $\sim +0.2$.

B.2 A synthetic model study

The parametric study of physical relations described in Appendix B.1 suggests that the most important factors determining the evolution of fracture aperture are the geomechanical fracture properties (*i.e.*, residual aperture, frictional drop and dilation angle). To create a reliable map of permeability in the fractured reservoir using the EPM or Oda's crack tensor theory, it is essential to identify the distribution and orientation of discrete fractures and to define the size of the representative element volume (REV) of the fractured domain in which the reservoir permeability is to be mapped. We build a synthetic forward DFN-MEQ-Permeability model to quantify the relationship between the induced MEQs and the permeability of the reservoir, and to explore how the mapped permeability varies with the selected size of the REV.

In the synthetic model, we set 300 penny-shaped discrete fractures at a prescribed depth of $3\ km$ within a reservoir with an edge dimension of 1500 m $\times$ 1500 m (Fig. B3**(a)**). The strike of these fractures are randomly oriented at azimuths (to North) within 30° to 150° and 210° to 330°, with arbitrary dip magnitudes within 0° to 90°. The lengths of fractures are statistically arranged from 20 m to 300 m (Fig. B3**(b)**), which can be described *via* the fracture length-frequency power law as follows,

$$n(l) = \rho_c \cdot l^{-\xi} \tag{B1}$$

where $n(l)$ is the density distribution of the number of fractures present in the interval $[l, l + dl]$; ρ_c is a fracture density constant and ξ is an exponent.

Assuming a gravitational lithostatic stress gradient of 24 MPa/km (2450 kg/m^3) and hydrostatic pore pressure gradient of 10 MPa/km, the total vertical stress on the synthetic reservoir is fixed at $S_v = 72$ MPa. We set three potential Andersonian (Anderson, 1905) stress regimes (normal faulting: $S_v = 72$ MPa, $S_{Hmax} = 63$ MPa, $S_{hmin} = 45$ MPa $P_p = 30$ MPa; strike-slip faulting: $S_{Hmax} = 75$ MPa, $S_v = 72$ MPa, $S_{hmin} = 45$ MPa; reverse faulting: $S_{Hmax} = 78$ MPa, $S_{hmin} = 75$ MPa, $S_v = 72$ MPa) for the fractured reservoir. Before fluid injection, the stress states in each faulting regime
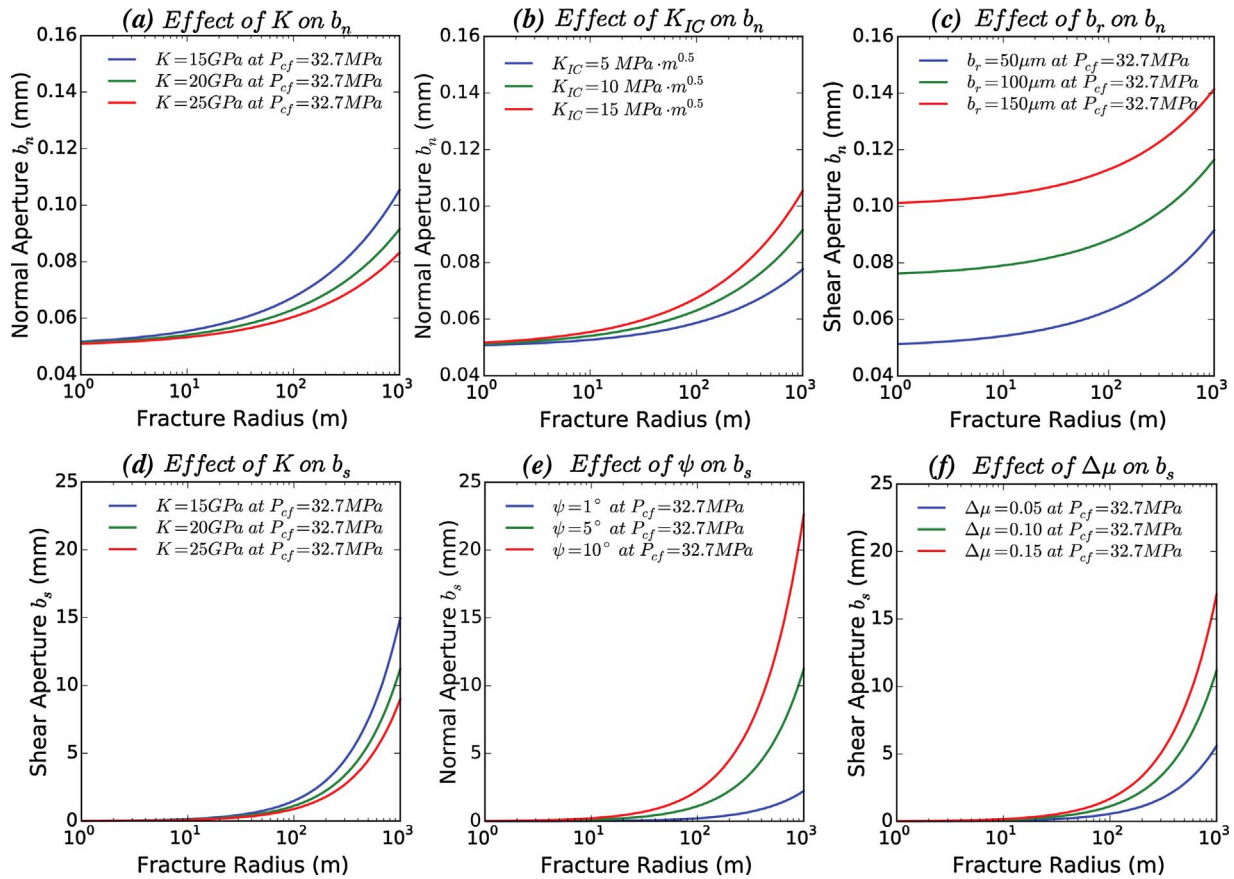
Fig. B2. Graph panel shows the geomechanical parameters that may affect the evolution of aperture in normal, b_n, and in shear, b_s. **(a)** Effect of bulk modulus K on normal aperture b_n; **(b)** Effect of fracture toughness K_{IC} on normal aperture b_n; **(c)** Effect of residual aperture b_r on normal aperture b_n; **(d)** Effect of bulk modulus K on shear aperture b_s; **(e)** Effect of fracture dilation angle ψ on shear aperture b_s; **(f)** Effect of frictional difference $\Delta\mu$ on shear aperture b_s.

are plotted in Fig. B4(c)–(e) . The fractures in the normal faulting and strike-slip faulting regimes are much closer to the Mohr-Coulomb failure than those of the reverse faulting regime, suggesting that the fractures in the normal and strike-slip faulting regimes will be most prone to fail by fluid injection. Based on observations from the World Stress Map, most current EGS projects are located in normal faulting or strike-slip faulting regime. Hence, in the following analysis, we particularly select the normal faulting stress regime where the maximum horizontal and minimum horizontal stresses are in the North-South and the East-West directions respectively. Moreover, the wellhead pressure is imposed on the entire domain rather than originating from a point source. The geomechanical parameters of fractures are listed in Table B2.

When a wellhead pressure of 5 MPa is applied to the fractured reservoir, the most favorably oriented fractures are reactivated first, as indicated in Fig. B4(a). The resulting seismic moment magnitudes range from $M_w = \sim -0.3$ to $\sim +2.4$. Increasing the wellhead pressure to 15 MPa (Fig. B4(b)) evidently reactivates the fractures that are less favorably oriented. Although the population of MEQs increases significantly due to the elevated fluid pressure, the variation of moment magnitudes remains within this confined range – this is a result of the fracture size distribution. It can be speculated that large moment magnitude seismic events are more likely to occur in the reservoir only where large-radius fractures are embedded. It is also noted that the apertures of fractures are enhanced by the seismic events and are proportional to the moment magnitudes.

The previous analysis implies that a zone within the reservoir with a high density of seismic events is expected to be more permeable. This prediction is examined by mapping the permeability of the synthetic reservoir after injection at wellhead pressures of 5 MPa and 15 MPa respectively and by employing both cubic law and Oda's crack tensor methods. The results obtained from these two methods (Figs. B5 and B6) indicate that the permeability is relatively high in the block where fractures are present. The evaluated permeability in each block is not constant but varies with the selected size of the REV. When the block size is increased, the hydraulic properties of fractures are averaged over a larger area, resulting in a declining magnitude of permeability in the block. The evaluated permeability from the cubic-law method in each block is slightly larger than that evaluated from Oda's crack tensor theory.

B.3 Discussion and summary

In reality, the in-situ stress conditions and observed MEQ data are far more complex than those assumed in the model. For the future prospect of this application method, three essential improvements are recommended to remove intrinsic limitations of the model: (1) Couple the real-time dynamic stress balance in the MEQ-perm coupled model. Based on the framework of this model, a rigorous DFN implemented mechanical model can
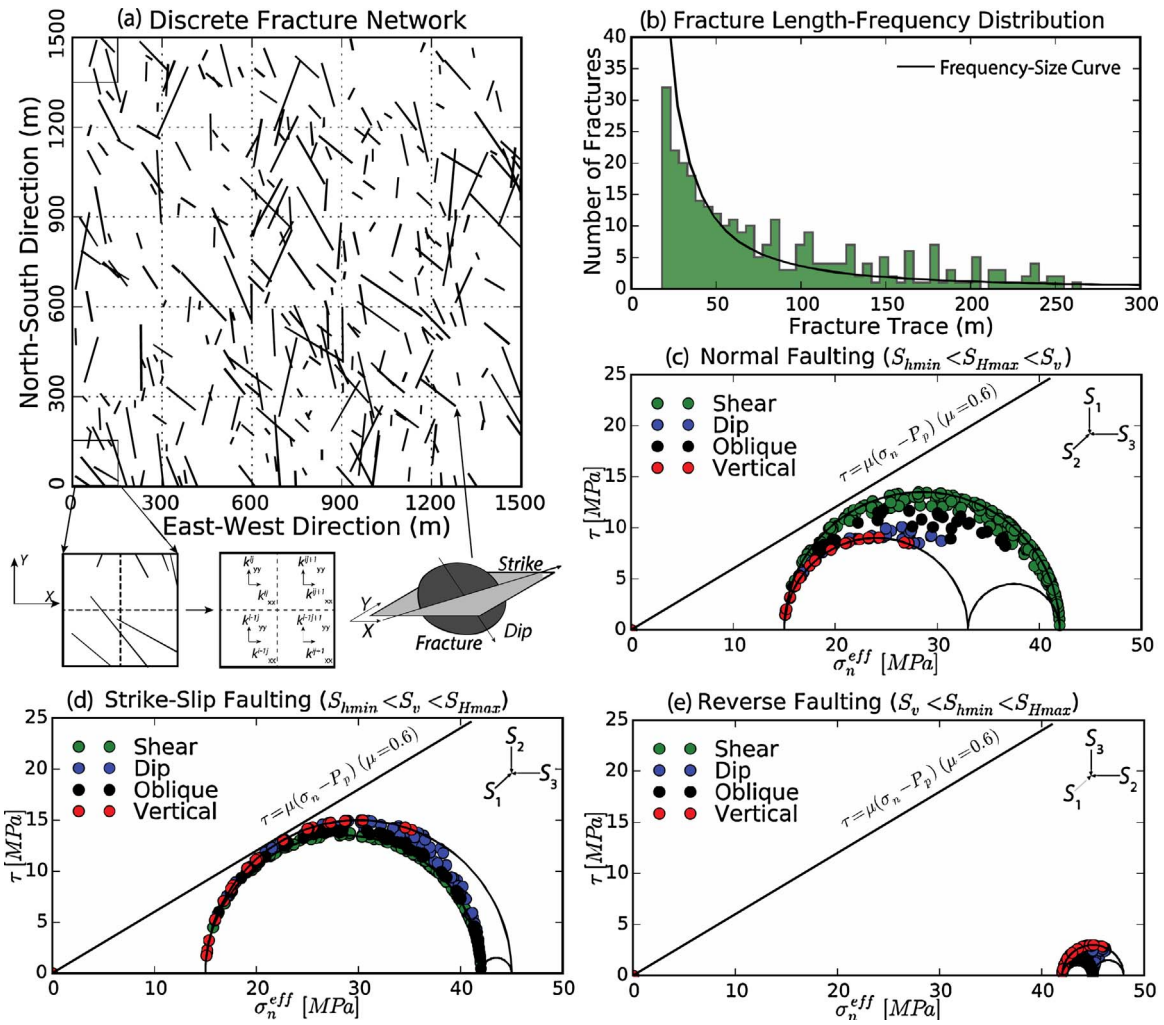
Fig. B3. (a) Generated 2D discrete fracture network where the fracture diameters cut the same plane; (b) Size-frequency distribution of generated fractures; (c)–(e) Mohr circles of discrete fractures subject to hydrostatic stresses of three faulting regimes at a depth of 3 km with known vertical stress gradient (normal faulting: S_v = 72 MPa, S_{Hmax} = 63 MPa, S_{hmin} = 45 MPa P_p = 30 MPa; strike-slip faulting: S_{Hmax} = 75 MPa, S_v = 72 MPa, S_{hmin} = 45 MPa; reverse faulting: S_{Hmax} = 78 MPa, S_{hmin} = 75 MPa, S_v = 72 MPa).
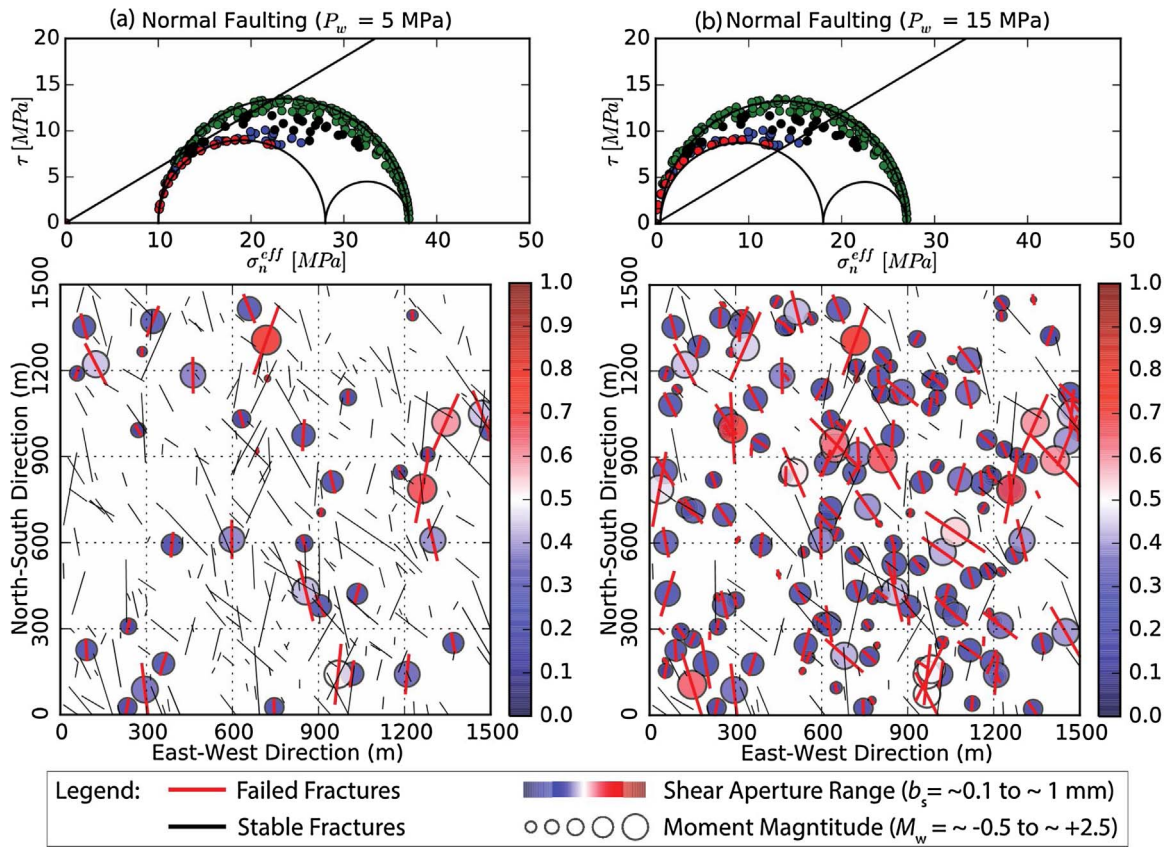
Fig. B4. (a) and **(b)** Mohr circles of discrete fractures in the domain that are respectively subject to a wellhead pressure of 5 MPa and 15 MPa in the normal faulting stress regime (S_v = 72 MPa, S_{Hmax} = 63 MPa, S_{hmin} = 45 MPa P_p = 30 MPa). Stable fractures and reactivated fractures are explicitly illustrated in the reservoir domain. The moment magnitude and the fracture apertures are correlated for each shear-reactivated fracture.

Table B2
Parameters Used in the Synthetic Model Analysis.

| Parameters	Symbol	Value	Units
Frictional drop	$\Delta\mu$	0.050	–
Vertical stress	S_v	72.0	MPa
Max-horizontal stress	S_H	63.0	MPa
Min-horizontal stress	S_h	45.0	MPa
Pore-pressure	P_0	30.0	MPa
Wellhead pressure	P_w	5, 15	MPa
Residual aperture	b_r	5.0e-5	m
Dilation angle	ψ	5.0	°
Bulk modulus	K	20.0	MPa
Poisson ratio	ν	0.25	–
Non-linear fracture stiffness	α_s	0.3	1/MPa
Power law scaling exponent	e	0.5	$m^{1/2}$
Constant stress intensity factor	K_{IC}	10.0	MPa $m^{1/2}$
REV size	L_{rev}	30, 60, 100	m
Fracture number	n	300	–
Fracture trace length	l	20 to 300	m
Matrix Permeability	k_{matrix}	1.0e-18	m^2
Source Plot Parameter	k_T	0	–
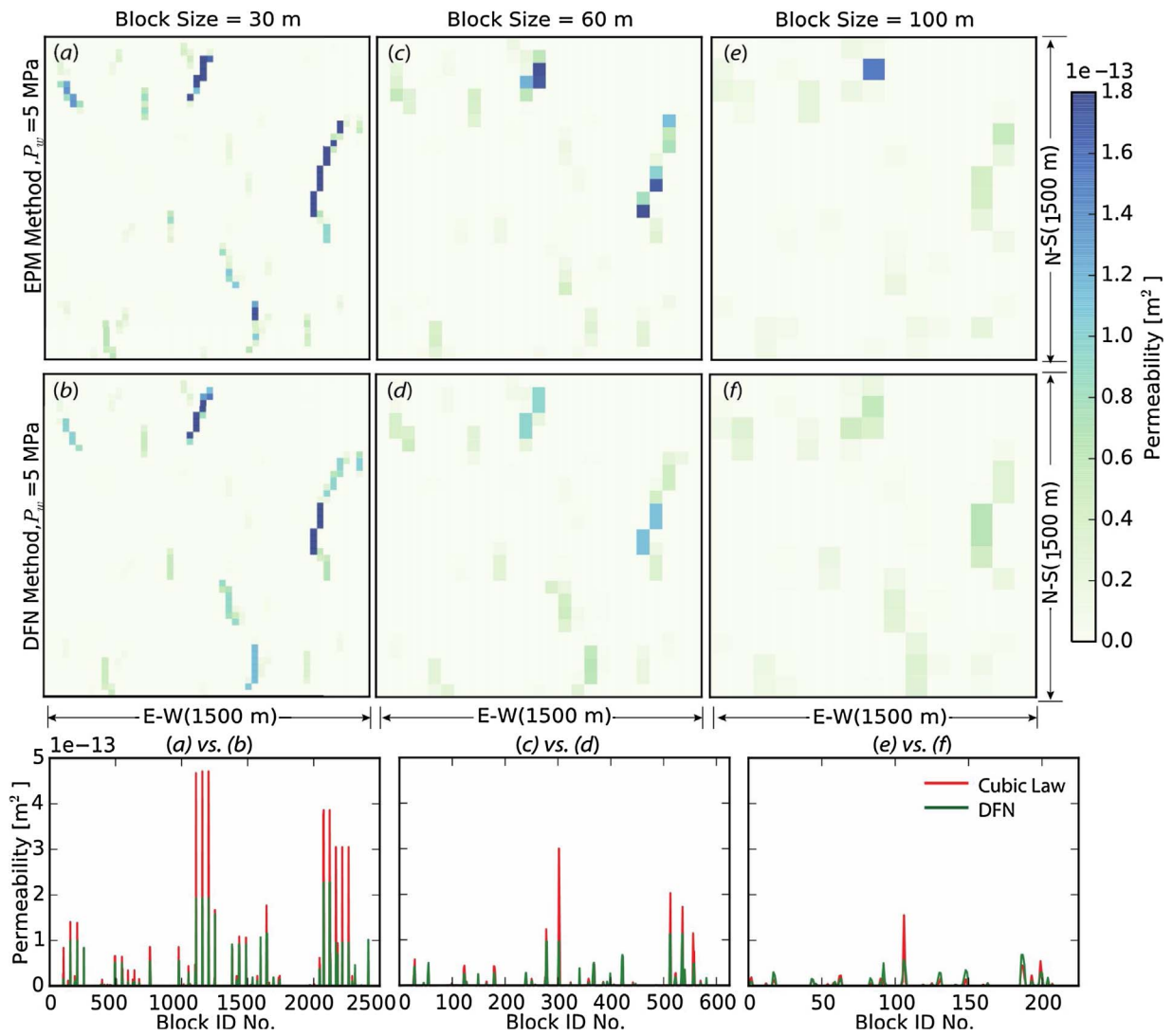
Fig. B5. Map of the estimated mean permeability of the synthetic fractured reservoir with different REV sizes. The reservoir is subject to a wellhead pressure at 5 MPa using the EPM method versus the DFN method. **(a)** and **(b)**: the comparison of permeability map of a small REV (30 m) by each method; **(c)** and **(d)**: the comparison of permeability map of a small REV (60 m) by each method; **(e)** and **(f)**: the comparison of permeability map of a small REV (100 m) by each method. The comparisons of permeability of each block are show in the lower portion of the diagram.
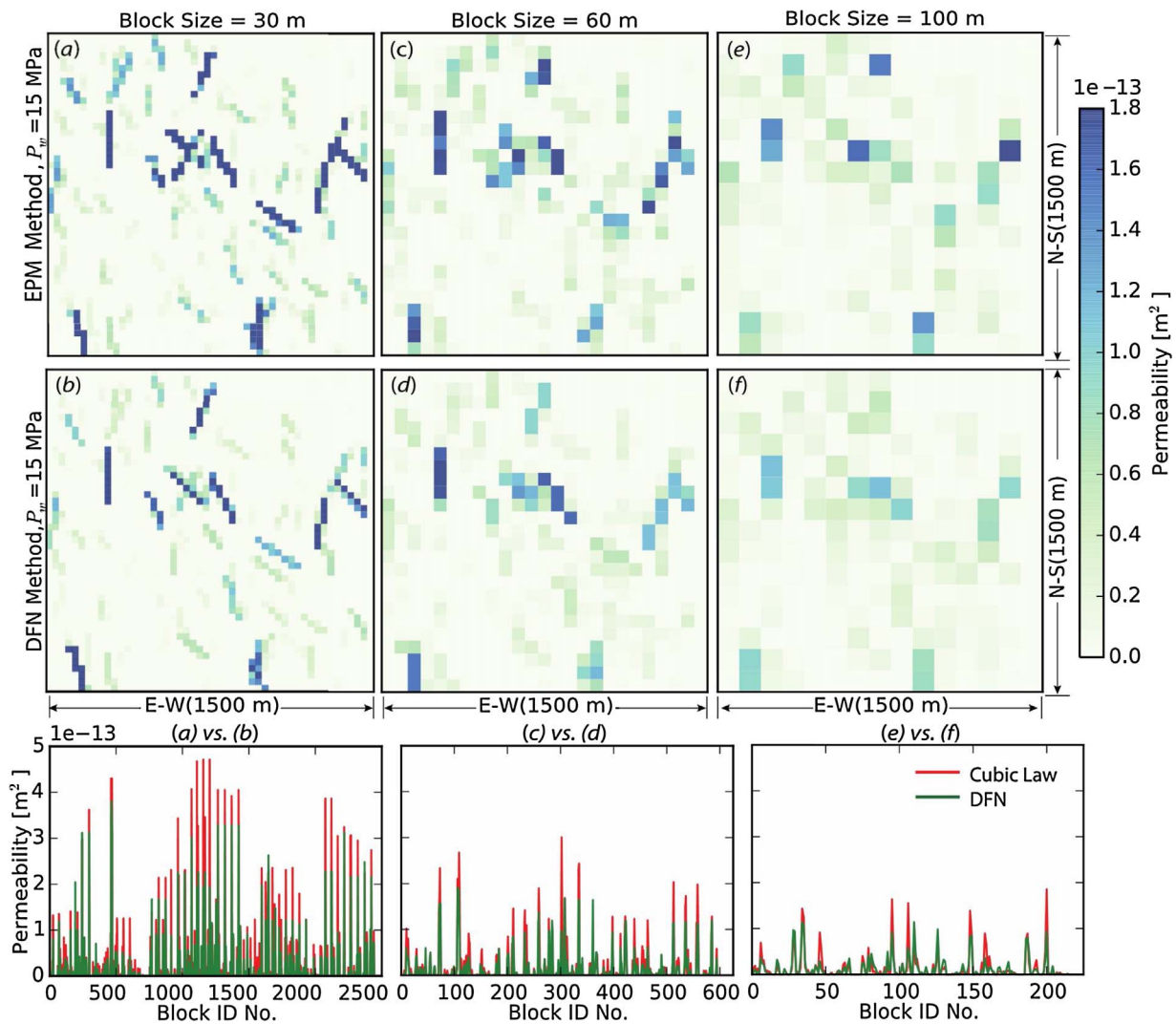
Fig. B6. Map of the estimated mean permeability of the synthetic fractured reservoir with different REV sizes. The reservoir is subject to a wellhead pressure at 15 MPa using the EPM method versus DFN method. **(a)–(b)**: the comparison of permeability map of a small REV (30 m) by each method; **(c)–(d)**: the comparison of permeability map of a small REV (60 m) by each method; **(e)–(f)**: the comparison of permeability map of a small REV (100 m) by each method. The comparisons of permeability of each block are show in the lower portion of the diagram.

be developed but this may be at the expenses of computational efficiency when applied at reservoir scale. (2) Understand the fundamental relationship between shear deformation and permeability evolution. This model employs a simple shear dilation – permeability enhancement relation. However, some laboratory and numerical experiments have revealed the contradictory observations that permeability decreases with shear slip due to the generated wear products or gouge (Vogler et al., 2016; Fang et al., 2017; Wang et al., 2017). In addition, thermal contraction induced aseismic deformation may play a significant role in changing fracture permeability in reservoir stimulation. This process may particularly occur during aseismic domain. These effects on the governing relationships are worth considering in the model. (3) Enhance the accuracy of the measured geophysical parameters. From the parametric analysis and the synthetic model study, the reliability of these methods is affected by the geomechanical properties, populations, location and orientations of fractures. These properties, for example, the frictional drop during fracture slip, the modulus of the matrix, and the residual fracture apertures can be measured in the laboratory. The population and spatial information of fractures can be confirmed from geophysical observations with high resolution.

References

Anderson, E.M., 1905. The dynamics of faulting. Trans. Edinburgh Geol. Soc. 8 (3), 387–402.

Barthélémy, J.F., Guiton, M.L.E., Daniel, J.M., 2009. Estimates of fracture density and uncertainties from well data. Int. J. Rock Mech. Min. Sci. 46 (3), 590–603. http://dx.doi.org/10.1016/j.ijrmms.2008.08.003.

Bonnet, E., Bour, O., Odling, N.E., Davy, P., Main, I., Cowie, P., Berkowitz, B., 2001. Scaling of fracture systems in geological media. Rev. Geophys. 39 (3), 347–383. http://dx.doi.org/10.1029/1999RG000074.

Bour, O., Davy, P., 1999. Clustering and size distributions of fault patterns: theory and measurements. Geophys. Res. Lett. 26 (13), 2001. http://dx.doi.org/10.1029/1999GL900419.

Breede, K., Dzebisashvili, K., Liu, X., Falcone, G., 2013. A systematic review of enhanced (or engineered) geothermal systems: past, present and future. Geotherm. Energy 1 (1), 4. http://dx.doi.org/10.1186/2195-9706-1-4.

Brune, J.N., 1970. Tectonic stress and the spectra of seismic shear waves from earthquakes. J. Geophys. Res. 75 (26), 4997–5009. http://dx.doi.org/10.1029/JB075i026p04997.

Bundschuh, J., Arriaga, M.C.S., 2010. Introduction to the Numerical Modeling of Groundwater and Geothermal Systems: Fundamentals of Mass, Energy and Solute Transport in Poroelastic Rocks. Taylor & Francis, Boca Raton.

Cladouhos, T.T., Petty, S., Callahan, O., Osborn, W., Hickman, S., Davatzes, N., 2011. The role of stress modeling in stimulation planning at the newberry volcano EGS demonstration project. Thirty Sixth Workshop on Geothermal Reservoir Engineering. Stanford University, Stanford, California vol. SGP-TR-191, p. 8.

Cladouhos, T.T., Petty, S., Swyer, M.W., Uddenberg, M.E., Grasso, K., Nordin, Y., 2016.

Results from newberry volcano EGS demonstration, 2010–2014. Geothermics 63, 44–61. http://dx.doi.org/10.1016/j.geothermics.2015.08.009.

Davatzes, N.C., Hickman, S.H., 2011. Preliminary analysis of stress in the newberry EGS well NWG 55-29. GRG Trans. 35, 323–332.

Dieterich, J.H., 1986. A model for the nucleation of earthquake slip. Earthquake Source Mechanics, vol. 37. AGU, Washington, DC, pp. 37–47.

Dieterich, J.H., 1992. Earthquake nucleation on faults with rate-and state-dependent strength. Tectonophysics 211 (1–4), 115–134. http://dx.doi.org/10.1016/0040-1951(92)90055-B.

Downie, R., Xu, J., Grant, D., Malpani, R., Viswanathan, A., 2013. Microseismic parameters help to calibrate complex hydraulic fracture models. World Oil (SPEC. SUPPL. MARC) 13–16.

Ellsworth, W.L., 2013. Injection-induced earthquakes. Science (80-) 341 (6142), 142–149. http://dx.doi.org/10.1126/science.1225942.

Elsworth, D., Goodman, R.E., 1986. Characterization of rock fissure hydraulic conductivity using idealized wall roughness profiles. Int. J. Rock Mech. Min. Sci. Geomech. Abstr. 23 (3), 233–243. http://dx.doi.org/10.1016/0148-9062(86)90969-1.

Fang, Y., den Hartog, S.A.M., Elsworth, D., Marone, C., Cladouhos, T., 2015. Anomalous distribution of microearthquakes in the Newberry Geothermal Reservoir: mechanisms and implications. Geothermics. http://dx.doi.org/10.1016/j.geothermics.2015.04.005.

Fang, Y., Elsworth, D., Wang, C., Ishibashi, T., Fitts, J.P., 2017. Frictional stability-permeability relationships for fractures in shales. J. Geophys. Res. Solid Earth 122, 1760–1776. http://dx.doi.org/10.1002/2016JB013435.

Foulger, G., Long, R.E., 1984. Anomalous focal mechanisms: tensile crack formation on an accreting plate boundary. Nature 310 (5972), 43–45.

Guglielmi, Y., Cappa, F., Avouac, J.-P., Henry, P., Elsworth, D., 2015. Seismicity triggered by fluid injection–induced aseismic slip. Science 348 (6240), 1224–1226. http://dx.doi.org/10.1126/science.aab0476.

Hudson, J.A., Pearce, R.G., Rogers, R.M., 1989. Source type plot for inversion of the moment tensor. J. Geophys. Res. 94 (B1), 765. http://dx.doi.org/10.1029/JB094iB01p00765.

Hummel, N., Shapiro, S.A., 2012. Microseismic estimates of hydraulic diffusivity in case of non-linear fluid-rock interaction. Geophys. J. Int. 188, 1441–1453. http://dx.doi.org/10.1111/j.1365-246X.2011.05346.x.

Ikari, M.J., Marone, C., Saffer, D.M., 2011. On the relation between fault strength and frictional stability. Geology 39 (1), 83–86. http://dx.doi.org/10.1130/g31416.1.

Ishibashi, T., Watanabe, N., Asanuma, H., Tsuchiya, N., 2016. Linking microearthquakes to fracture permeability evolution. Geofluids Special Thematic Issues Crustal Permeability. pp. 49–64.

Julian, B.R., Miller, A.D., Foulger, G.R., 1998. Non-double-couple earthquakes 1. Theory. Rev. Geophys. 36 (4), 525. http://dx.doi.org/10.1029/98RG00716.

Majer, E.L., Baria, R., Stark, M., Oates, S., Bommer, J., Smith, B., Asanuma, H., 2007. Induced seismicity associated with enhanced geothermal systems. Geothermics 36 (3), 185–222. http://dx.doi.org/10.1016/j.geothermics.2007.03.003.

Maxwell, S.C., Urbancic, T.I., 2001. The role of passive microseismic monitoring in the instrumented oil field. Lead. Edge 20 (6), 636. http://dx.doi.org/10.1190/1.1439012.

Maxwell, S.C., Rutledge, J., Jones, R., Fehler, M., 2010. Petroleum reservoir characterization using downhole microseismic monitoring. Geophysics 75 (5), 75A129. http://dx.doi.org/10.1190/1.3477966.

Miller, A.D., Foulger, G.R., Julian, B.R., 1998. Non-double-couple earthquakes 2. Observations. Rev. Geophys. 36 (4), 551. http://dx.doi.org/10.1029/98RG00717.

Murphy, H.D., Tester, J.W., Grigsby, C.O., Potter, R.M., 1981. Energy extraction from fractured geothermal reservoirs in low-permeability crystalline rock. J. Geophys. Res. 86 (B8), 7145. http://dx.doi.org/10.1029/JB086iB08p07145.

Nicholson, C., Wesson, R.L., 1990. Earthquake hazard associated with deep well injection: a report to the U.S. Environmental Protection Agency. US Geol. Surv. Bull. 1951 74pp.

Oda, M., 1982. Fabric tensor for discontinuous geological materials. Soils Found. 22 (4), 96–108.

Oda, M., 1984. Similarity rule of crack geometry in statistically homogeneous rock masses. Mech. Mater. 3 (2), 119–129. http://dx.doi.org/10.1016/0167-6636(84)90003-6.

Oda, M., 1985. Permeability tensor for discontinuous rock masses. Geotechnique 35 (4), 483–495.

Olson, J.E., 2003. Sublinear scaling of fracture aperture versus length: an exception or the rule? J. Geophys. Res. Solid Earth 108 (B9), 2413. http://dx.doi.org/10.1029/2001JB000419.

Ortega, O.J., Marrett, R.A., Laubach, S.E., 2006. A scale-independent approach to fracture intensity and average spacing measurement. Am. Assoc. Pet. Geol. Bull. 90 (2), 193–208. http://dx.doi.org/10.1306/08250505059.

Peng, Z., Gomberg, J., 2010. An integrated perspective of the continuum between earthquakes and slow-slip phenomena. Nat. Geosci. 3, 599–607. http://dx.doi.org/10.1038/ngeo940.

Polak, A., Elsworth, D., Yasuhara, H., Grader, A.S., Halleck, P.M., 2003. Permeability reduction of a natural fracture under net dissolution by hydrothermal fluids. Geophys. Res. Lett. 30 (20). http://dx.doi.org/10.1029/2003gl017575. Artn 2020.

Priest, S.D., Hudson, J.A., 1981. Estimation of discontinuity spacing and trace length using scanline surveys. Int. J. Rock Mech. Min. Sci. Geomech. Abstr. 18 (3), 183–197. http://dx.doi.org/10.1016/0148-9062(81)90973-6.

Priest, S.D., Priest, S.D., Hudson, J.A., Hudson, J.A., 1976. Discontinuity spacings in rock. Int. J. Rock Mech. Min. Sci. Geomech. Abstr. 13 (5), 135–148. http://dx.doi.org/10.1016/0148-9062(76)90818-4.

Rinaldi, A.P., Rutqvist, J., Sonnenthal, E.L., Cladouhos, T.T., 2015. Coupled THM modeling of hydroshearing stimulation in tight fractured volcanic rock. Transp. Porous Media 108 (1), 131–150. http://dx.doi.org/10.1007/s11242-014-0296-5.

Rutqvist, J., Tsang, C.F., 2003. Analysis of thermal-hydrologic-mechanical behavior near an emplacement drift at Yucca Mountain. J. Contam. Hydrol. 62–63, 637–652. http://dx.doi.org/10.1016/S0169-7722(02)00184-5.

Rutqvist, J., Tsang, C.F., Tsang, Y., 2004. Analysis of stress and moisture induced changes in fractured rock permeability at the Yucca mountain drift scale test. In: In: Ove, S. (Ed.), Elsevier Geo-Engineering Book Series, vol. 2. Elsevier, pp. 161–166.

Scholz, C.H., 1998. Earthquakes and friction laws. Nature 391 (6662), 37–42. http://dx.doi.org/10.1038/34097.

Shapiro, S.A., Huenges, E., Borm, G., 1997. Estimating the crust permeability from fluid-injection-induced seismic emission at the KTB site. Geophys. J. Int. 131 (2), F15–F18. http://dx.doi.org/10.1111/J.1365-246x.1997.Tb01215.X.

Shapiro, S.A., Dinske, C., Rothert, E., 2006. Hydraulic-fracturing controlled dynamics of microseismic clouds. Geophys. Res. Lett. 33 (14). http://dx.doi.org/10.1029/2006gl026365. Artn L14312.

Snow, D.T., 1969. Anisotropic permeability of fractured media. Water Resour. Res. 5 (6). http://dx.doi.org/10.1029/Wr005i006p01273. 1273–&.

Stein, S., Wysession, M., 2009. An Introduction to Seismology, Earthquakes, and Earth Structure. Wiley.

Suckale, J., 2009. Induced seismicity in hydrocarbon fields. Adv. Geophys. 51 (09), 1976–1984. http://dx.doi.org/10.1016/S0065-2687(09)05107-3.

Terakawa, T., Zoporowski, A., Galvan, B., Miller, S.A., 2010. High-pressure fluid at hypocentral depths in the L'Aquila region inferred from earthquake focal mechanisms. Geology 38 (11), 995–998. http://dx.doi.org/10.1130/g31457.1.

Terakawa, T., Miller, S.A., Deichmann, N., 2012. High fluid pressure and triggered earthquakes in the enhanced geothermal system in Basel, Switzerland. J. Geophys. Res. Solid Earth Res. 117 (B7), B07305. http://dx.doi.org/10.1029/2011JB008980.

Tsang, Y.W., Witherspoon, P.A., 1981. Hydromechanical behavior of a formable rock fracture subject to normal stress. J. Geophys. Res. 86 (B10), 9287–9298.

van der Elst, N.J., Brodsky, E.E., 2010. Connecting near-field and far-field earthquake triggering to dynamic strain. J. Geophys. Res. Solid Earth 115 (B7), B07311. http://dx.doi.org/10.1029/2009JB006681.

van der Elst, N.J., Savage, H.M., Keranen, K.M., Abers, G.A., 2013. Enhanced remote earthquake triggering at fluid-injection sites in the midwestern United States. Science (80-.) 341 (6142), 164–167. http://dx.doi.org/10.1126/science.1238948.

Vogler, D., Amann, F., Bayer, P., Elsworth, D., 2016. Permeability evolution in natural fractures subject to cyclic loading and gouge formation. Rock Mech. Rock Eng. 49 (9), 3463–3479. http://dx.doi.org/10.1007/s00603-016-1022-0.

Wang, C., Elsworth, D., Fang, Y., 2017. Influence of weakening minerals on ensemble strength and slip stability of faults. J. Geophys. Res. Solid Earth 122, 7090–7110. http://dx.doi.org/10.1002/2016JB013687.

Warren, J.E., Root, P.J., 1963. The behavior of naturally fractured reservoirs. Soc. Pet. Eng. J. 3 (3), 245–255. http://dx.doi.org/10.2118/426-PA.

Witherspoon, P.A., Wang, J.S.Y., Iwai, K., Gale, J.E., 1980. Validity of Cubic Law for fluid flow in a deformable rock fracture. Water Resour. Res. 16 (6), 1016–1024. http://dx.doi.org/10.1029/WR016i006p01016.

Zeeb, C., Gomez-Rivas, E., Bons, P.D., Blum, P., 2013. Evaluation of Sampling methods for fracture network characterization using Outcrops. Am. Assoc. Pet. Geol. Bull. 97 (9), 1545–1566. http://dx.doi.org/10.1306/02131312042.

Zoback, M.D., Gorelick, S.M., 2012. Earthquake triggering and large-scale geologic storage of carbon dioxide. Proc. Natl. Acad. Sci. U. S. A. 109 (26), 10164–10168. http://dx.doi.org/10.1073/Pnas.1202473109.